An artificial spring component mode synthesis method for built-up structures

Jie Deng, Oriol Guasch, Laurent Maxit, Nansha Gao

An artificial spring component mode synthesis method for built-up structures

Jie Deng[a,*], Oriol Guasch[b], Laurent Maxit[c], Nansha Gao[d,**]

[a]*Key Laboratory of Ocean Acoustic and Sensing, School of Marine Science and Technology, Northwestern Polytechnical University, Xi'an 710072, China*
[b]*GTM - Grup de Recerca en Tecnologies Mèdia, La Salle, Universitat Ramon Llull C/ Quatre Camins 30, 08022 Barcelona, Catalonia (Spain)*
[c]*INSA–Lyon, Laboratoire Vibrations-Acoustique (LVA) 25 bis, av. Jean Capelle, F-69621 Villeurbanne Cedex, France*
[d]*Key Laboratory of Unmanned Underwater Vehicle, School of Marine Science and Technology, Northwestern Polytechnical University, Xi'an 710072, China*

Abstract

In this paper, we develop a component mode synthesis method that relies on artificial springs to connect the subsystems of a built-up structure. The modal behaviour of the subsystems can be computed using different approaches, from analytical to numerical methods, depending on their complexity. The advantage of using artificial springs to link the subsystems is that one can model them with the Rayleigh-Ritz method, which is problematic in component mode synthesis. As known, the approximating functions must satisfy the system boundary conditions and the use of artificial springs avoids this difficulty. Moreover, and as in other component mode synthesis approaches, one can build reduced-order models at the subsystem level to significantly diminish the dimensions of the entire built-up structure, resulting in substantial reduction of the computational cost when performing numerical simulations. The method is first presented for the simple case of two axially connected beams. Two more complex cases are then addressed. The first one deals with two beams connected at right angles and the second one deals with an internal floor attached to a cylindrical shell, which reminds of some aeronautical structures. The performance of the method is carefully analysed and validated against finite element simulations.

Keywords: Component mode synthesis, Built-up systems, Substructures, Artificial springs, Coupling

1. Introduction

Aeronautical, naval, and civil transportation structures can become very complex and determining their vibration field often becomes a daunting task. One way to simplify such situation is that of dynamic sub-

*Corresponding Author: dengjie@nwpu.edu.cn
**Corresponding Author: gaonansha@nwpu.edu.cn

structuring. The issue has been around for decades and in the sixties of the last century, efforts were placed on finding options to recover the modal behaviour of large structures from the modal behaviour of their components. Hurty [1, 2] and Gladwell [3] put forward the basis of component mode synthesis (CMS). The components' modes were divided into rigid-body, constraint, and normal modes, resulting into three-block mass, stiffness and damping matrices. Typically, in sub-structuring analysis continuity at joints gives rise to compatibility equations for the displacements as well as force equilibrium conditions [4], enabling substructure coupling through a transformation matrix [2]. Yet in the Rayleigh-Ritz framework, the equilibrium condition is often substituted by the compatibility of the displacement derivatives (e.g., rotational angles). Further progress was made by Guyan [5], who took advantage of projecting the internal degrees of freedom with no external forces onto the outer ones, where exterior loads were applied. Craig and Bampton [6] improved the mode synthesis theory by introducing the fixed interface hypothesis, laying the foundation for typical fixed-fixed interface methods. The dual modal formulation to link components with very different impedance mismatch was also established by that time [7–9]. Interestingly, the dual modal formulation was later extended to couple substructures in the mid-high frequency range using a stress-displacement approach, within the framework of the statistical modal energy distribution analysis [10–12]. Recently, the dual formulation has been also applied to account for the vibrations of multiple subsystems connected at a junction in the case of strong impedance mismatch [13], while a reformulated energy-based Craig-Bampton has been proposed for linked subsystems with low impedance mismatch [14].

Certainly, a large number of papers dealing with CMS approaches have been published in the last decades and, in recent years, free-free [15–17], free-fixed [18] and fixed-fixed [14] interface conditions have been addressed. Uncertainty propagation in CMS models has also received much attention [19–21] and some CMS methods for built-up systems with nonlinearities [22, 23] and damping [24, 25] have been developed. Mode selection strategies have been suggested for model order reduction [26], according to non-physical, semi-physical, and physical subspace reduction methods [27] (see e.g., the semi-physical interior mode ranking in [28]). The big advantage of CMS methods is that it is not only possible to recover the global behaviour of a built-up structure from that of its components, but also to build a reduced-order model for the system by truncating the set of modes considered for each substructure. Applications cover a large variety of problems, from recovering the response of a washing machine using reduced models of its cabinet and legs [29], to investigating the nonlinear aeroservoelastic behaviour of a three-dimensional supersonic aircraft [30], among many others. The reader is referred to [4, 31] for some complete reviews on CMS methods.

While the CMS is well established for numerical approaches involving some type of mesh, like the finite

element method (FEM), see e.g. [32–35], this is not the case for the Rayleigh-Ritz method (RRM). The RRM turns to be useful as an alternative to FEM in problems with simple geometries that require very fine meshes (e.g., acoustic black holes in mechanics, see [36, 37] and references therein). However, substructuring in the RRM is difficult because the approximating functions need to explicitly satisfy the substructure boundary conditions. In addition, and as far as the authors know, no strategy to build reduced-order models in the framework of the RRM has been presented to date. This constitutes the main goal of this paper.

A few strategies have been suggested to address the problem of fulfilment of the boundary conditions by the approximating functions in the RRM. One option is to directly modify the function basis to that aim, see e.g., [38–42] where wavelets and Gaussian functions were used as shape functions. Yet, this is only possible for very simple structures. Alternatively, a well-known and more flexible technique to assemble substructures within the RRM that avoids the boundary conditions problem is the penalty method [43] (also referred to as the artificial spring method). This approach has proved useful in many circumstances [44–47]. The idea is to impose a penalty function into the system Lagrangian that allows the shape functions to describe the displacement field even if they do not fulfil the compatibility conditions [48]. The penalty function represents the coupling potential energy of artificial springs connecting the substructures. Courant suggested the use of artificial stiffness parameters having very large magnitude so that a rigid constraint could be approximately modelled by a restraint [43]. Subsequently, Ilanko introduced the use of negative stiffness in addition to positive stiffness, to bound the error of the penalty approach [49]. Remarkably, negative stiffness with a finite value can be realized in some practical situations [50]. Moreover, Ilanko also used inertial penalty to speed up the convergence of the method [51]. The advantage of using artificial springs is that of allowing the simulation of arbitrary constraints, exemplified by plate [52] and cylindrical shell [53, 54] boundary conditions, connections between plates and resonators [55, 56], and beam [57] and plate-shell coupling systems [58, 59]. Another useful approach in the RRM is the Lagrangian multiplier method (LMM) [60, 61]. In the LMM, a proper combination of approximating functions is forced to satisfy the boundary conditions instead of requiring the functions to satisfy the constraints individually. However, the LMM leads to larger dimension problems, a point we want to avoid herein. Finally, and very recently, a nullspace approach [62] has been proposed that presents some advantages with respect to the penalty and LMM methods. The method has proved successful for beam systems [63], including the case of periodic boundary conditions [64], but it is yet at its early initial stages.

It is the main goal of this paper to develop a CMS approach in the framework of the artificial spring Rayleigh-Ritz method that could yield reduced-order models for the vibration of large systems. The modal

behaviour of the latter is recovered from the modes of the substructures, which can be truncated to a certain order. The penalty function in the Lagrangian arising from the contribution of the potential energy of the artificial coupling springs incorporates the mode truncation as the displacements get projected onto the substructure modal basis. The suggested method will be hereafter designated as the artificial spring component mode synthesis (ASCMS) method, and it provides reduced-order models for built-up systems whose substructures (components) have been characterized by means of the RRM. Besides, it is to be noted that hybrid approaches in which different methods are used for different subsystems also fit well in the ASCMS framework. For instance, in buildings, the walls and the floors could be represented by analytical plate modes whereas some internal structures could be represented by FEM. As said, this can be advantageous for substructures requiring very fine FEM meshes like the centres of mechanical acoustic black holes (see e.g., [65–67]). It should be noted that the ASCMS method is not just a mere combination of the Rayleigh-Ritz method and the CMS. Though the use of artificial spring method has been extensively applied (see [68–71], among others), to the best of the authors knowledge it has never been developed to produce global reduced-order models, and the convergence and computational efficiency dependence on coupling strength and modal truncation has not been analysed before.

The paper is organized as follows. In section 2 we introduce the theoretical framework of the ASCMS, which expands the potential of the traditional artificial spring technique. To facilitate the explanations, the simple case of two beams connected at one of their ends by translational or rotational springs is considered. A careful analysis follows in section 3, where the convergence of the method depending on the artificial spring stiffness, coupling strength, and model order reduction gets analysed and compared with FEM models. Once validated, the ASCMS is applied to more complex cases in section 4. The first one consists of two beams connected at right angles. The second one is more industrially oriented and comprises a cylindrical shell with an internal floor partition. Such configuration can be typically found in aeronautical and underwater vehicle designs. Conclusions close the paper in section 5.

2. Theoretical framework of the ASCMS method

In this section, we will present the theoretical basis of the ASCMS method. To that purpose and for the ease of exposition, the case of a compound beam consisting of two connected short beams of distinct thickness is considered. First, the standard artificial spring method in the RMM framework will be revisited for the example at hand. Then, the proposed ASCMS will be applied to the example to highlight the differences between both approaches. It is believed that starting with this simple case will help the reader

to easily understand the key features of the ASCMS.

As shown in Fig. 1a, we consider two thin Euler-Bernouilli beams fully coupled at the joint $x = x_1$, with Beam 1 having length L_1 and thickness h_1, and Beam 2 having length L_2 and thickness h_2. It is to be noted that for simplicity only bending motion is taken into account in this example. We can separate Beam 1 and Beam 2 at the junction and reconnect them through a translational spring, k_1, and a rotational one, k_2 (see Fig. 1b). The first spring controls the displacement difference between beams at the joint, while the second one accounts for the difference in rotational angle. If we let $k_1 \to +\infty$ and $k_2 \to +\infty$, the fully coupled situation is recovered. Note that this is an asymptotic modelling process to mimic the boundary conditions. Excessive stiffness values may lead to ill-conditioned matrices. The simultaneous use of positive and negative stiffness values can bound the resulting error [51, 72].

Before introducing the ASCMS strategy, let us briefly describe the general procedure for computing the modes of the two-beam structure using the traditional artificial spring technique. The bending displacements of the beams, $w_1(x,t)$ and $w_2(x,t)$, are expanded in terms of approximating functions

$$w_1(x,t) = \boldsymbol{a}_1^\top(t)\boldsymbol{\zeta}_1(x) = \boldsymbol{\zeta}_1^\top(x)\boldsymbol{a}_1(t), \tag{1}$$

$$w_2(x,t) = \boldsymbol{a}_2^\top(t)\boldsymbol{\zeta}_2(x) = \boldsymbol{\zeta}_2^\top(x)\boldsymbol{a}_2(t), \tag{2}$$

where subscripts 1 and 2 respectively refer to the variables of Beams 1 and 2. $\boldsymbol{\zeta}_i (i = 1, 2)$ stand for the basis vectors expanding the general space, and $\boldsymbol{a}_i (i = 1, 2)$ represent the associated time dependent weights. The size n_i of $\boldsymbol{\zeta}_i$ determines the approximating order of the i-th substructure.

As detailed in Fig. 2a, the next step of the artificial spring technique is to build the Lagrangian of the system from the kinetic and potential energies of the beams as well as from the potential energy stored in the artificial springs k_1 and k_2.

The kinetic energies of Beams 1 and 2 can be written as

$$\begin{aligned} E_{\text{kin1}} =& \frac{1}{2}\int_0^{L_1} \rho h_1 \dot{w}_1^2 \mathrm{d}x = \frac{1}{2}\int_0^{L_1} \rho h_1 \left(\dot{\boldsymbol{a}}_1^\top \boldsymbol{\zeta}_1 \boldsymbol{\zeta}_1^\top \dot{\boldsymbol{a}}_1\right) \mathrm{d}x \\ =& \frac{1}{2}\dot{\boldsymbol{a}}_1^\top \left[\int_0^{L_1} \rho h_1 \left(\boldsymbol{\zeta}_1 \boldsymbol{\zeta}_1^\top\right) \mathrm{d}x\right] \dot{\boldsymbol{a}}_1 \equiv \frac{1}{2}\dot{\boldsymbol{a}}_1^\top \boldsymbol{M}_1 \dot{\boldsymbol{a}}_1, \end{aligned} \tag{3}$$

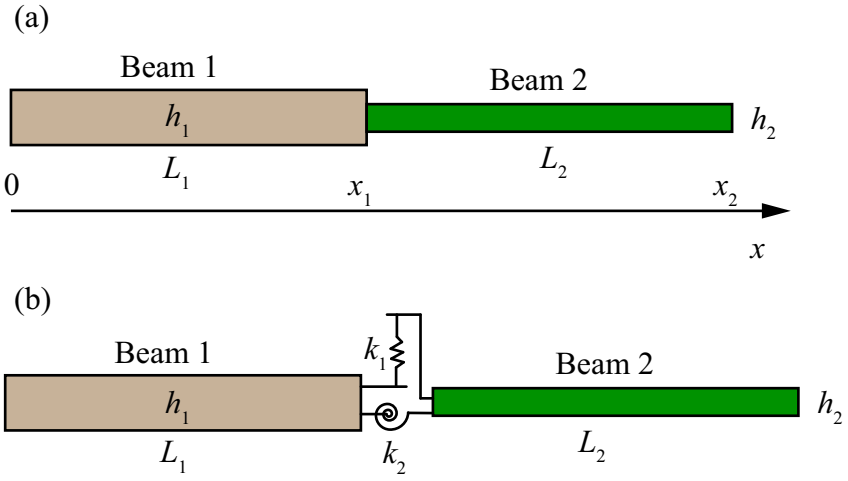

Figure 1: Illustration of (a) two fully coupled beams with different thickness, and (b) the two beam substructures connected by artificial springs, in which k_1 and k_2 respectively control the bending displacement and rotational angle differences at the joint. Artificial springs are only applied at the connected boundaries of each beam while global boundary conditions (zero external force and moment in this case) are imposed at the non-connected ends of the beams. Note also that the axial vibration is not considered and when $k_1 \to +\infty$ and $k_2 \to +\infty$ case (a) is recovered.

and

$$E_{\text{kin2}} = \frac{1}{2}\int_{L_1}^{L_2} \rho h_2 \dot{w}_2^2 \mathrm{d}x \equiv \frac{1}{2}\dot{\boldsymbol{a}}_2^\top \boldsymbol{M}_2 \dot{\boldsymbol{a}}_2, \tag{4}$$

where ρ is the density, and in the last equalities we have identified the corresponding mass matrices.

On the other hand, the potential energies of the beams are given by

$$\begin{aligned} E_{\text{pot1}} =& \frac{1}{2}\int_0^{L_1} EI_1 \left(\partial_{xx}^2 w_1\right)^2 \mathrm{d}x = \frac{1}{2}\int_0^{L_1} EI_1 \left(\boldsymbol{a}_1^\top \partial_{xx}^2 \boldsymbol{\zeta}_1 \partial_{xx}^2 \boldsymbol{\zeta}_1^\top \boldsymbol{a}_1\right) \mathrm{d}x \\ =& \frac{1}{2}\boldsymbol{a}_1^\top \left[\int_0^{L_1} EI_1 \left(\partial_{xx}^2 \boldsymbol{\zeta}_1 \partial_{xx}^2 \boldsymbol{\zeta}_1^\top\right) \mathrm{d}x\right] \boldsymbol{a}_1 \equiv \frac{1}{2}\boldsymbol{a}_1^\top \boldsymbol{K}_1 \boldsymbol{a}_1, \end{aligned} \tag{5}$$

and

$$E_{\text{pot2}} = \frac{1}{2}\int_{L_1}^{L_2} EI_2 \left(\partial_{xx}^2 w_2\right)^2 \mathrm{d}x \equiv \frac{1}{2}\boldsymbol{a}_2^\top \boldsymbol{K}_2 \boldsymbol{a}_2, \tag{6}$$

in which $EI_i = Eh_i^3/12 (i = 1, 2)$ represents the bending stiffness. Note that we have also identified the stiffness matrices of the beams in the above expressions.

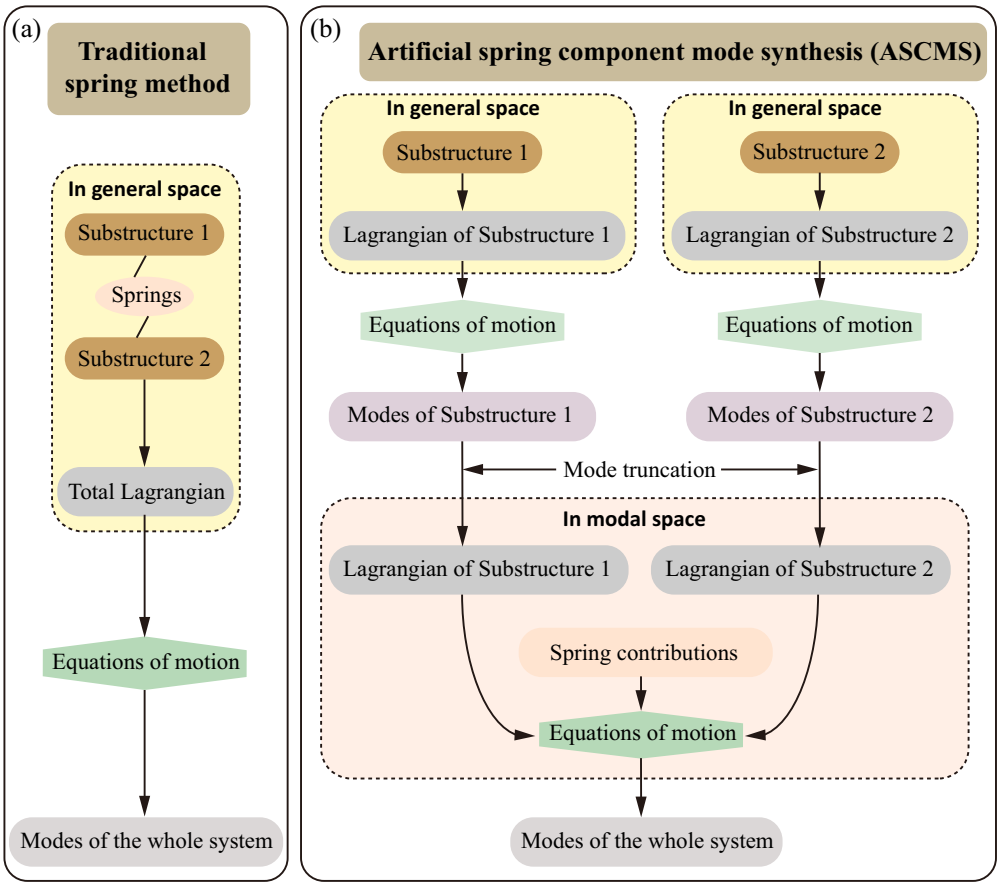

Figure 2: (a) The modelling procedure of the traditional artificial spring method for a built-up structure, where the Lagrangian is obtained in the general spatial domain. (b) The proposed framework for the artificial spring component modal synthesis (ASCMS) method. In this case the modes of each substructure are computed and truncated, and their corresponding Lagrangians are expressed in the modal space before getting assembled to obtain the global equations of motion.

At the junction between the two beams the following coupling equations must be satisfied,

$$\lim_{k_1 \to +\infty} w_1(L_1) - w_2(L_1) = 0, \qquad \lim_{k_2 \to +\infty} \partial_x w_1(L_1) - \partial_x w_2(L_1) = 0. \tag{7}$$

Therefore, the potential energy stored in the translational spring is given by

$$
\begin{aligned}
E_{\mathrm{spr1}} =& \frac{1}{2} k_1 [w_1(L_1) - w_2(L_1)]^2 \\
=& \frac{1}{2} k_1 [w_1^2(L_1) - w_1(L_1) w_2(L_1) - w_2(L_1) w_1(L_1) + w_2^2(L_1)] \\
=& \frac{1}{2} k_1 [\boldsymbol{a}_1^\top \boldsymbol{\zeta}_1(L_1) \boldsymbol{\zeta}_1^\top(L_1) \boldsymbol{a}_1 - \boldsymbol{a}_1^\top \boldsymbol{\zeta}_1(L_1) \boldsymbol{\zeta}_2^\top(L_1) \boldsymbol{a}_2 - \boldsymbol{a}_2^\top \boldsymbol{\zeta}_2(L_1) \boldsymbol{\zeta}_1^\top(L_1) \boldsymbol{a}_1 + \boldsymbol{a}_2^\top \boldsymbol{\zeta}_2(L_1) \boldsymbol{\zeta}_2^\top(L_1) \boldsymbol{a}_2] \\
=& \frac{1}{2} \begin{bmatrix} \boldsymbol{a}_1 \\ \boldsymbol{a}_2 \end{bmatrix}^\top \begin{bmatrix} k_1 \boldsymbol{\zeta}_1(L_1) \boldsymbol{\zeta}_1^\top(L_1) & -k_1 \boldsymbol{\zeta}_1(L_1) \boldsymbol{\zeta}_2^\top(L_1) \\ -k_1 \boldsymbol{\zeta}_2(L_1) \boldsymbol{\zeta}_1^\top(L_1) & k_1 \boldsymbol{\zeta}_2(L_1) \boldsymbol{\zeta}_2^\top(L_1) \end{bmatrix} \begin{bmatrix} \boldsymbol{a}_1 \\ \boldsymbol{a}_2 \end{bmatrix} \\
\equiv& \frac{1}{2} \begin{bmatrix} \boldsymbol{a}_1 \\ \boldsymbol{a}_2 \end{bmatrix}^\top \boldsymbol{K}_{\mathrm{spr1}} \begin{bmatrix} \boldsymbol{a}_1 \\ \boldsymbol{a}_2 \end{bmatrix},
\end{aligned} \tag{8}
$$

and that in the rotational spring by,

$$
\begin{aligned}
E_{\mathrm{spr2}} =& \frac{1}{2} k_2 [\partial_x w_1(L_1) - \partial_y w_2(L_1)]^2 \\
=& \frac{1}{2} \begin{bmatrix} \boldsymbol{a}_1 \\ \boldsymbol{a}_2 \end{bmatrix}^\top \begin{bmatrix} k_2 \partial_x \boldsymbol{\zeta}_1(L_1) \partial_x \boldsymbol{\zeta}_1^\top(L_1) & -k_2 \partial_x \boldsymbol{\zeta}_1(L_1) \partial_x \boldsymbol{\zeta}_2^\top(L_1) \\ -k_2 \partial_x \boldsymbol{\zeta}_2(L_1) \partial_x \boldsymbol{\zeta}_1^\top(L_1) & k_2 \partial_x \boldsymbol{\zeta}_2(L_1) \partial_x \boldsymbol{\zeta}_2^\top(L_1) \end{bmatrix} \begin{bmatrix} \boldsymbol{a}_1 \\ \boldsymbol{a}_2 \end{bmatrix} \\
\equiv& \frac{1}{2} \begin{bmatrix} \boldsymbol{a}_1 \\ \boldsymbol{a}_2 \end{bmatrix}^\top \boldsymbol{K}_{\mathrm{spr2}} \begin{bmatrix} \boldsymbol{a}_1 \\ \boldsymbol{a}_2 \end{bmatrix}.
\end{aligned} \tag{9}
$$

Again, the coupling stiffness matrices for each spring have been defined in the last equalities of Eqs. (8) and (9).

From Eqs. (3) to (9) we can construct the total two-beam structure Lagrangian as,

$$
\begin{aligned}
\mathscr{L} =& (E_{\mathrm{kin1}} + E_{\mathrm{kin2}}) - (E_{\mathrm{pot1}} + E_{\mathrm{pot2}} + E_{\mathrm{spr1}} + E_{\mathrm{spr2}}) \\
=& \frac{1}{2} \begin{bmatrix} \dot{\boldsymbol{a}}_1 \\ \dot{\boldsymbol{a}}_2 \end{bmatrix}^\top \begin{bmatrix} \boldsymbol{M}_1 & \boldsymbol{0} \\ \boldsymbol{0} & \boldsymbol{M}_2 \end{bmatrix} \begin{bmatrix} \dot{\boldsymbol{a}}_1 \\ \dot{\boldsymbol{a}}_2 \end{bmatrix} - \frac{1}{2} \begin{bmatrix} \boldsymbol{a}_1 \\ \boldsymbol{a}_2 \end{bmatrix}^\top \left(\begin{bmatrix} \boldsymbol{K}_1 & \boldsymbol{0} \\ \boldsymbol{0} & \boldsymbol{K}_2 \end{bmatrix} + \boldsymbol{K}_{\mathrm{spr1}} + \boldsymbol{K}_{\mathrm{spr2}} \right) \begin{bmatrix} \boldsymbol{a}_1 \\ \boldsymbol{a}_2 \end{bmatrix} \\
\equiv& \frac{1}{2} \dot{\boldsymbol{a}}^\top \boldsymbol{M} \dot{\boldsymbol{a}} - \frac{1}{2} \boldsymbol{a}^\top \boldsymbol{K} \boldsymbol{a}.
\end{aligned} \tag{10}
$$

Finally, applying the Euler-Lagrange equations $\partial_t(\partial_{\dot{\boldsymbol{a}}} \mathscr{L}) - \partial_{\boldsymbol{a}} \mathscr{L} = 0$ to Eq. (10) and setting $\boldsymbol{a} =$

$\hat{\boldsymbol{A}}\exp(\mathrm{i}\omega t)$ we get the equations of motion of the total system in the frequency domain,

$$\left(\boldsymbol{K}-\omega^2\boldsymbol{M}\right)\hat{\boldsymbol{A}}=\boldsymbol{0}. \tag{11}$$

Via Eq. (11) one can recover the modes of the two-beam built-up structure. The dimension of the model will be the summation of that of Beam 1 plus that of Beam 2, namely $n_{\text{total}}=n_1+n_2$.

Up to this point no novelty has been introduced. This is how the standard artificial spring method would proceed to solve the problem of the two rigidly connected beams within the RRM. However, for a more complex example than the current one n_{total} can become prohibitively large. Therefore, it would be convenient to build a reduced-order model in which the modes of the global system (two beams) could be recovered from a small set of individual modes of each beam. This is the essential of the CMS methods presented in the introduction. However, CMS methods have not been yet developed for the RRM. This is what the ASCMS provides: a methodology to compute a limited number of individual modes for each beam using the RRM and then assemble them to get the modes of the global system by resorting to artificial springs. The ASCMS strategy is summarized in Fig. 2b and it is to be compared with the standard spring method in Fig. 2a, in which no model reduction is considered. Let us next see how the ASCMS works for the two-beam example.

The n_i modes of each individual beam can be obtained from

$$\left(\boldsymbol{K}_i-\omega_i^2\boldsymbol{M}_i\right)\overline{\boldsymbol{A}}_i=\boldsymbol{0},\quad i=1,2, \tag{12}$$

where ω_i are the modal frequencies and $\overline{\boldsymbol{A}}_i$ the modal vectors for Beam i. The stiffness and mass matrices in Eq. (12) have dimensions $n_i\times n_i$. Next, let us construct the truncated eigen-vector matrices $\overline{\boldsymbol{P}}_i=[\overline{\boldsymbol{A}}_{i,1},\overline{\boldsymbol{A}}_{i,2},\overline{\boldsymbol{A}}_{i,3},...,\overline{\boldsymbol{A}}_{i,\overline{n}_i}]$, where $\overline{\boldsymbol{A}}_{i,j}$ stands for the j-th normalized eigen-vector of Beam i and $\overline{n}_i\ll n_i$. The generalized mass and stiffness matrices become

$$\begin{aligned}\overline{\boldsymbol{M}}_i&=\overline{\boldsymbol{P}}_i^{\top}\boldsymbol{M}_i\overline{\boldsymbol{P}}_i,\quad i=1,2,\\ \overline{\boldsymbol{K}}_i&=\overline{\boldsymbol{P}}_i^{\top}\boldsymbol{K}_i\overline{\boldsymbol{P}}_i,\quad i=1,2,\end{aligned} \tag{13}$$

with dimensions $\overline{n}_i\times\overline{n}_i$. At this point, there is freedom in choosing how to compute the modes in each substructure. For instance, one could use an analytical or semi-analytical method for Beam 1 and FEM for Beam 2 (that would be reasonable if instead of Beam 2 we had a more complex substructure).

By projecting the weights in Eqs.(1) and (2) into the modal space we obtain,

$$\boldsymbol{a}_i = \overline{\boldsymbol{P}}_i \boldsymbol{\varepsilon}_i, \quad i = 1, 2, \tag{14}$$

where $\boldsymbol{\varepsilon}_i$ are the vectors of modal participation factors. Taking Eq. (14) into Eqs. (3) and (4) allows one to compute the kinetic energy of the two beams as

$$\begin{aligned}
E_{\text{kin}} &= \frac{1}{2}\dot{\boldsymbol{a}}_1^\top \boldsymbol{M}_1 \dot{\boldsymbol{a}}_1 + \frac{1}{2}\dot{\boldsymbol{a}}_2^\top \boldsymbol{M}_2 \dot{\boldsymbol{a}}_2 \\
&= \frac{1}{2}(\overline{\boldsymbol{P}}_1 \dot{\boldsymbol{\varepsilon}}_1)^\top \boldsymbol{M}_1 (\overline{\boldsymbol{P}}_1 \dot{\boldsymbol{\varepsilon}}_1) + \frac{1}{2}(\overline{\boldsymbol{P}}_2 \dot{\boldsymbol{\varepsilon}}_2)^\top \boldsymbol{M}_2 (\overline{\boldsymbol{P}}_2 \dot{\boldsymbol{\varepsilon}}_2) \\
&= \frac{1}{2}\dot{\boldsymbol{\varepsilon}}_1^\top (\overline{\boldsymbol{P}}_1^\top \boldsymbol{M}_1 \overline{\boldsymbol{P}}_1) \dot{\boldsymbol{\varepsilon}}_1 + \frac{1}{2}\dot{\boldsymbol{\varepsilon}}_2^\top (\overline{\boldsymbol{P}}_2^\top \boldsymbol{M}_2 \overline{\boldsymbol{P}}_2) \dot{\boldsymbol{\varepsilon}}_2 \\
&\equiv \frac{1}{2}\dot{\boldsymbol{\varepsilon}}_1^\top \overline{\boldsymbol{M}}_1 \dot{\boldsymbol{\varepsilon}}_1 + \frac{1}{2}\dot{\boldsymbol{\varepsilon}}_2^\top \overline{\boldsymbol{M}}_2 \dot{\boldsymbol{\varepsilon}}_2 \\
&= \frac{1}{2}\begin{bmatrix} \dot{\boldsymbol{\varepsilon}}_1 \\ \dot{\boldsymbol{\varepsilon}}_2 \end{bmatrix}^\top \begin{bmatrix} \overline{\boldsymbol{M}}_1 & \boldsymbol{0} \\ \boldsymbol{0} & \overline{\boldsymbol{M}}_2 \end{bmatrix} \begin{bmatrix} \dot{\boldsymbol{\varepsilon}}_1 \\ \dot{\boldsymbol{\varepsilon}}_2 \end{bmatrix} \\
&\equiv \frac{1}{2}\dot{\boldsymbol{\varepsilon}}^\top \overline{\boldsymbol{M}} \dot{\boldsymbol{\varepsilon}},
\end{aligned} \tag{15}$$

where in the last line we have defined the reduced mass matrix of the system (identity for mass-normalized eigenvectors). Likewise, we get for the potential energy of the two beams,

$$\begin{aligned}
E_{\text{pot}} &= \frac{1}{2}\boldsymbol{a}_1^\top \boldsymbol{K}_1 \boldsymbol{a}_1 + \frac{1}{2}\boldsymbol{a}_2^\top \boldsymbol{K}_2 \boldsymbol{a}_2 \\
&= \frac{1}{2}(\overline{\boldsymbol{P}}_1 \boldsymbol{\varepsilon}_1)^\top \boldsymbol{K}_1 (\overline{\boldsymbol{P}}_1 \boldsymbol{\varepsilon}_1) + \frac{1}{2}(\overline{\boldsymbol{P}}_2 \boldsymbol{\varepsilon}_2)^\top \boldsymbol{K}_2 (\overline{\boldsymbol{P}}_2 \boldsymbol{\varepsilon}_2) \\
&= \frac{1}{2}\boldsymbol{\varepsilon}_1^\top (\overline{\boldsymbol{P}}_1^\top \boldsymbol{K}_1 \overline{\boldsymbol{P}}_1) \boldsymbol{\varepsilon}_1 + \frac{1}{2}\boldsymbol{\varepsilon}_2^\top (\overline{\boldsymbol{P}}_2^\top \boldsymbol{K}_2 \overline{\boldsymbol{P}}_2) \boldsymbol{\varepsilon}_2 \\
&\equiv \frac{1}{2}\boldsymbol{\varepsilon}_1^\top \overline{\boldsymbol{K}}_1 \boldsymbol{\varepsilon}_1 + \frac{1}{2}\boldsymbol{\varepsilon}_2^\top \overline{\boldsymbol{K}}_2 \boldsymbol{\varepsilon}_2 \\
&= \frac{1}{2}\begin{bmatrix} \boldsymbol{\varepsilon}_1 \\ \boldsymbol{\varepsilon}_2 \end{bmatrix}^\top \begin{bmatrix} \overline{\boldsymbol{K}}_1 & \boldsymbol{0} \\ \boldsymbol{0} & \overline{\boldsymbol{K}}_2 \end{bmatrix} \begin{bmatrix} \boldsymbol{\varepsilon}_1 \\ \boldsymbol{\varepsilon}_2 \end{bmatrix} \\
&\equiv \frac{1}{2}\boldsymbol{\varepsilon}^\top \overline{\boldsymbol{K}} \boldsymbol{\varepsilon},
\end{aligned} \tag{16}$$

with $\overline{\boldsymbol{K}}$ being the reduced (diagonal) stiffness matrix. We have now reduced-order models for the two beams but they are still uncoupled. Therefore, we finally need to consider the energy stored in the artificial springs,

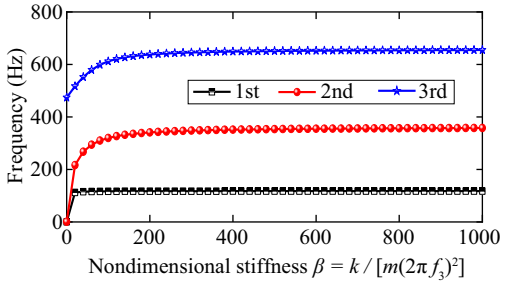

Figure 3: Influence of the artificial spring stiffness on the first three modal frequencies of the two-beam model, to see how convergence depends on the spring stiffness value. Here $m = 1$ stands for the normalized modal mass and f_3 for the 3-rd eigenfrequency of Beam 2.

which can be obtained as

$$\begin{aligned} E_{\text{spr}} &= \frac{1}{2}\begin{bmatrix} \boldsymbol{a}_1 \\ \boldsymbol{a}_2 \end{bmatrix}^\top \boldsymbol{K}_{\text{spr1}} \begin{bmatrix} \boldsymbol{a}_1 \\ \boldsymbol{a}_2 \end{bmatrix} + \frac{1}{2}\begin{bmatrix} \boldsymbol{a}_1 \\ \boldsymbol{a}_2 \end{bmatrix}^\top \boldsymbol{K}_{\text{spr2}} \begin{bmatrix} \boldsymbol{a}_1 \\ \boldsymbol{a}_2 \end{bmatrix} \\ &= \frac{1}{2}\begin{bmatrix} \boldsymbol{\varepsilon}_1 \\ \boldsymbol{\varepsilon}_2 \end{bmatrix}^\top \begin{bmatrix} \overline{\boldsymbol{P}}_1 & \boldsymbol{0} \\ \boldsymbol{0} & \overline{\boldsymbol{P}}_2 \end{bmatrix}^\top (\boldsymbol{K}_{\text{spr1}} + \boldsymbol{K}_{\text{spr2}}) \begin{bmatrix} \overline{\boldsymbol{P}}_1 & \boldsymbol{0} \\ \boldsymbol{0} & \overline{\boldsymbol{P}}_2 \end{bmatrix} \begin{bmatrix} \boldsymbol{\varepsilon}_1 \\ \boldsymbol{\varepsilon}_2 \end{bmatrix} \\ &\equiv \frac{1}{2}\boldsymbol{\varepsilon}^\top \overline{\boldsymbol{K}}_{\text{coup}} \boldsymbol{\varepsilon}, \end{aligned} \tag{17}$$

with $\overline{\boldsymbol{K}}_{\text{coup}}$ being the truncated spring coupling stiffness matrix.

From Eqs. (15)-(17) we can build the Lagrangian of the system and once applied the Euler-Lagrange equations and assuming $\boldsymbol{\varepsilon} = \hat{\boldsymbol{\varepsilon}}\exp(\mathrm{i}\omega t)$, get the eigenvalue problem

$$\left(\overline{\boldsymbol{K}} + \overline{\boldsymbol{K}}_{\text{coup}} - \omega^2 \overline{\boldsymbol{M}}\right)\hat{\boldsymbol{\varepsilon}} = \boldsymbol{0}. \tag{18}$$

Note that this is a reduced-order version of the problem in Eq. (11) and relies on the knowledge of the truncated eigenmodes of each substructure (beams), see Fig. 2b.

3. Convergence of the ASCMS

Having presented the basics of ASCMS on a simple example and before dealing with more complex ones, it would be convenient to see how the convergence of the method depends on several factors. In particular, we are interested in how to choose the values of the stiffness of the artificial spring and how this affects the results. It is also worth investigating the influence of the coupling force, which can be related to the thickness ratio of the two beams. Finally, and as usual, the effects of modal truncation should be determined.

Let us start analyzing the influence of the spring stiffness values. For the numerical tests the two beams are assumed to be made of steel with density $\rho = 7800$ kg/m^3 and Young's modulus $E = 210$ GPa. As for the geometry, Beam 1 has length $L_1 = 0.3$ m and thickness $h_1 = 0.008$ m, while Beam 2 has $L_2 = 0.2$ m and $h_2 = 0.004$ m. Gaussians are used as basis functions ζ_i appearing in the mass and stiffness matrices of the system. The procedure to obtain solutions to systems Eq. (10) and Eq. (18) by resorting to Gaussians in the framework of the Rayleigh-Ritz method is referred to as the Gaussian expansion method (GEM), see [65, 66] for details. Comparisons with FEM simulations are hereafter performed to validate the ASCMS approach.

Let us start examining the influence of the stiffness of the artificial coupling springs. As mentioned at the beginning of section 2, the spring stiffness should be chosen so that $k_1 \to +\infty$ and $k_2 \to +\infty$ to ensure full coupling at the junction. In Appendix A, we provide a simple example showing how to select the stiffness value k of an artificial spring that ensures that two substructures are rigidly coupled for frequencies above the eigenfrequencies of the substructures. In particular, it is shown that the artificial spring stiffness should satisfy $k \gg \frac{|\omega_1^2 - \omega_2^2|}{2}$. For simplicity and safety, one can then choose $k = \frac{\beta}{2}\max[\omega_1^2, \omega_2^2]$, with ω_1 and ω_2 respectively being the highest modal frequencies of Beams 1 and 2 and β a factor to be determined. On the other hand, and as in CMS strategies applied to finite element methods, the additional constraints also reduce the number of degrees of freedom (see Appendix A again). To find proper stiffness values for the artificial springs, one can gradually increase them until a convergent solution is achieved. This process is illustrated in Fig. 3, where the eigenfrequencies of the first three global modes of the two-beam system are plotted against non-dimensional spring stiffness values. As one could expect, the modal frequencies increase with stiffness until $\beta \geq 200$, where they become stable. Even though this is only validated for the first three modes in Fig. 3, the condition $\beta = k/[m(2\pi f_n)^2] \geq 200$ holds true for guaranteeing the convergence when n subsystem modes are considered. In other words, the ASCMS is capable of simulating the full coupling condition taking $\beta \geq 200$.

On the other hand, in classical CMS approaches, the criteria to choose free boundary conditions for the substructures (free-interface CMS) or fixed ones (fixed-interface CMS) depends on the coupling strength at the junction. For strong coupling, the free-interface CMS is selected while the fixed-interface CMS is chosen otherwise. The coupling strength is negatively correlated with $|r - 1|$, where $r = h_2/h_1$ represents, in our case, the beam thickness ratio at the interface. Because in its current formulation the ASCMS corresponds to a free-interface method, it is worthwhile testing the influence of the coupling strength on the convergence of the results. To check that, we have fixed $h_1 = 0.008$ m but changed the value of h_2. Five cases have

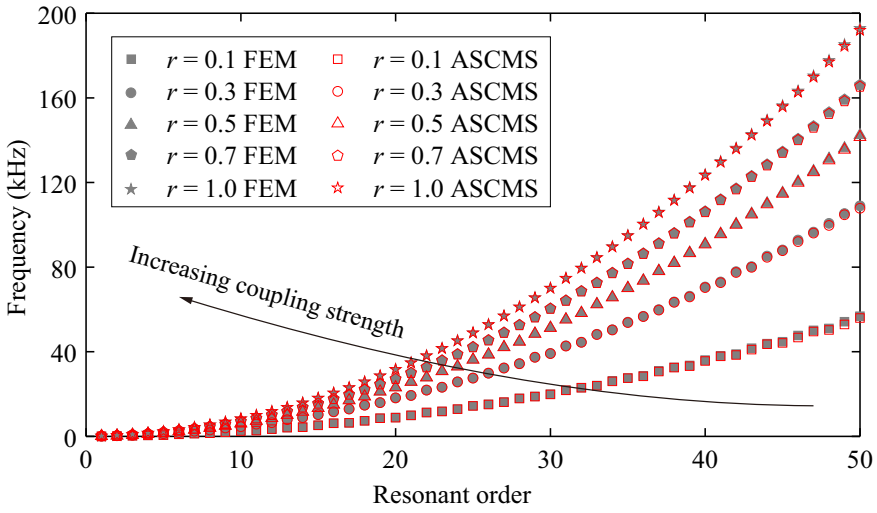

Figure 4: Comparison of the modal frequencies obtained with the proposed ASCMS method and the reference FEM model. The focus is placed on examining the effects of changing the thickness ratio $r = h_2/h_1$, to see how convergence is influenced by the coupling strength of the substructures. $r = 0.1$ corresponds to weak coupling, while $r = 1$ indicates strong coupling.

been examined, namely $r = [0.1, 0.3, 0.5, 0.7, 1.0]$. These cases have been also simulated using FEM for comparison. Fig. 4 presents the modal frequencies for the first fifty global orders for the five values of r. As observed in the figure, the matching between the FEM solutions and the ASCMS ones is extremely good. Furthermore, in Fig. 5 we have depicted the 20-th modal shape of the synthesized structure, with Fig. 5a - Fig. 5e respectively corresponding to $r = [0.1, 0.3, 0.5, 0.7, 1.0]$. It is seen that when the thickness ratio is small (i.e., weak coupling, say $r = 0.1$) Beam 1 barely vibrates. The right boundary of Beam 1 can be approximately regarded as free. As opposed, the left end of Beam 2 should be treated as fixed. Notwithstanding, when $r \to 1$ the coupling between beams gradually strengthens and the vibration of Beam 1 progressively intensifies. Again, it is important to observe that the ASCMS results closely resemble those of FEM.

It has been explained in the previous section that the main goal of the ASCMS is to get a modal reduced-order model that alleviates the computational cost of the whole system. Therefore, it is of interest checking how mode truncation affects the problem solution. The order of the reduced model is dictated by the number of eigenvectors chosen in Eq. (14), which gets reflected in the size of Eq. (18). Suppose that we are concerned in solving the system up to the 20-th mode eigenfrequency and that we use 50 modes to that purpose. The 20-th resonant mode has frequency $f_{20} = 18852$ Hz and for convenience, we have defined the non-dimensional frequency $\alpha = f/f_{20}$. In Fig. 6, the modal participation factors are drawn against α at each modal frequency of the two beams, for $r = [0.1, 0.5, 1.0]$. As observed, the participation of Beam 1 increases

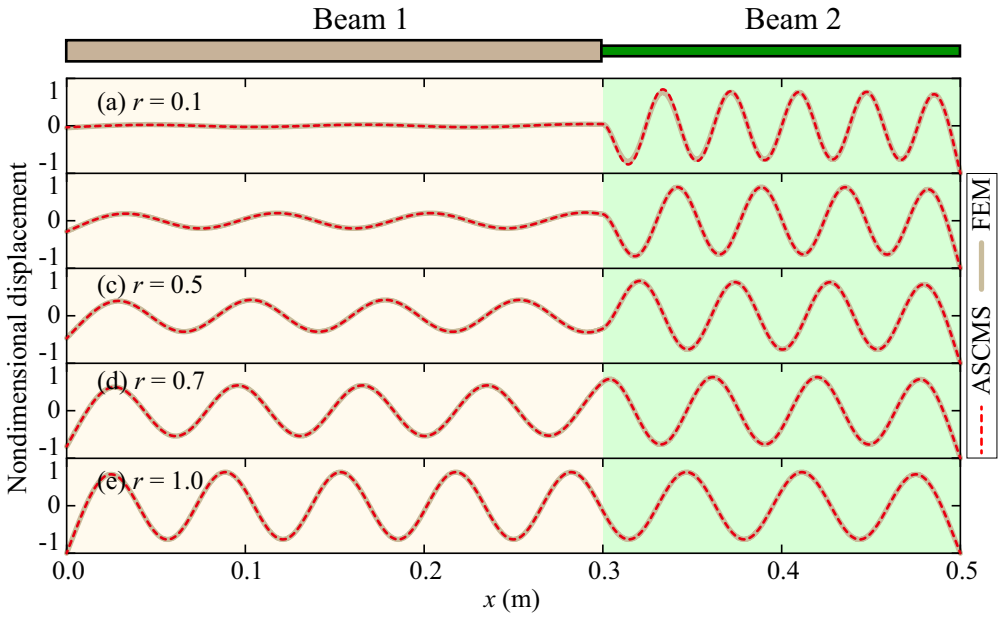

Figure 5: Comparison of the 20-th modal shapes computed with GEM and FEM for (a)-(e) different thickness ratios $r = h_2/h_1$. The region $0 < x < 0.3$ m corresponds to Beam 1, while $0.3 < x < 0.5$ m is for Beam 2. $r = 0.1$ designates weak coupling, while $r = 1$ indicates strong coupling.

with r, which is consistent with the conclusions from Fig. 5. Most importantly, the participation factors mostly locate near $\alpha = 1$. Modes for $\alpha < 1$ are also perceptible but modes with $\alpha \gg 1$ hardly contribute to

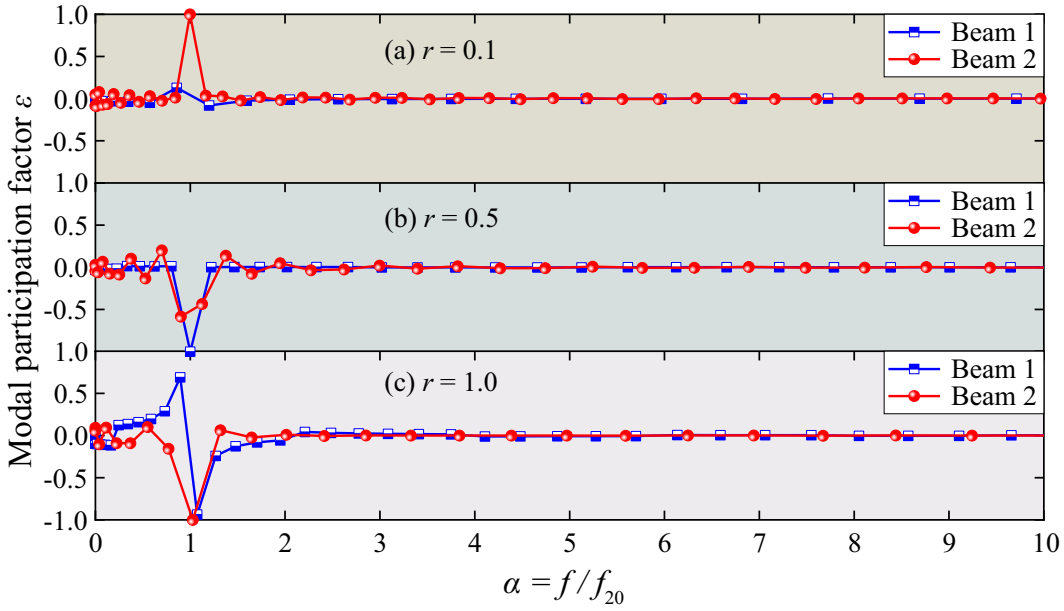

Figure 6: Modal participation factors (ε) of the modes of Beam 1 and Beam 2 to synthesize the 20th mode of the built-up structure. (a)-(c) ε for different coupling strength $r = h_2/h_1$. $r = 0.1$ corresponds to weak coupling, while $r = 1$ indicates strong coupling. For the ease of exposition, the abscissa is normalized to the 20th modal frequency, f_{20}, of the built-up structure.

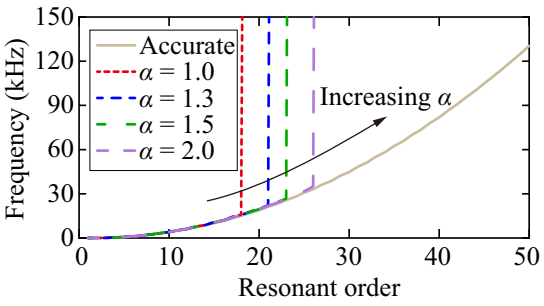

Figure 7: Highest modal frequency of the built-up structure when using different mode truncation values, α, to reconstruct the 20-th synthesized mode with $f_{20} = 18852$ Hz. The most accurate brown curve has been reconstructed using 50 modes for each substructure to simulate the situation $\alpha \to +\infty$.

the synthesis, whether the coupling strength r is strong ($r = 1$) or weak ($r = 0.1$). In general, high-order resonant modes can be reasonably eliminated. The final issue is to quantify how many modes should be used for the synthesis. This is shown in Fig. 7. There, we represent the modal frequencies synthesized with different values of α. The brown line corresponds to the most accurate case, where 50 modes have been used to emulate the situation $\alpha \to +\infty$. It is seen that for $\alpha = 1$ we are unable to reach the target mode (i.e., the 20-th mode) but for $\alpha = [1.3, 1.5, 2.0]$ that is recovered without problem. For the ASCMS approach it suffices to take modes in $[0, \alpha f_n]$ ($\alpha = 1.3 \sim 2.0$) to synthesize the n-th mode with modal frequency f_n. Finally, let us remark that the computational time before modal truncation was 0.315 s, while after truncation (taking $\alpha = 2$) it became 0.1224 s. The latter is less than the half of the former, showing the computational benefits of the ASCMS. All the simulations in this paper are performed on the core AMD 5950X.

4. Further applications of the ASCMS

After having introduced and validated the basics of the ASCMS approach by means of the bending motion of two beams connected in the axial direction, in this section we will consider some more complex cases. The first concerns the two beams of the previous example but now connected at right angles. Then, to examine the performance of the proposed ASCMS method in more complex structures, we will focus on the case of a cylindrical shell with a coupled internal floor. Such a structure is often found in aeronautical and naval applications (e.g., in underwater vehicles).

4.1. Application 1: two beams connected at right angles

Let us next consider two beams connected at right angles, see Fig. 8. In this case, it does not suffice to limit the analysis to bending motion and in-plane vibrations have to be considered as well. This is because

there will be conversion between the two types of waves at the joint between beams. The synthesis procedure will be first presented, followed by the results and numerical validations against finite element simulations.

4.1.1. Synthesis procedure

We proceed analogously to the case of the two axially connected beams, but now expanding the in-plane displacement $u_i(x_i,t)$, $x_i = x, y$, $i = 1,2$, and the bending one $w_i(x_i,t)$, $x_i = x, y$, $i = 1,2$, in terms of approximating function vectors $\boldsymbol{\chi}_i(x_i)$ and $\boldsymbol{\zeta}_i(x_i)$,

$$u_1(x,t) = \boldsymbol{a}_1^\top(t)\boldsymbol{\chi}_1(x), \quad w_1(x,t) = \boldsymbol{b}_1^\top(t)\boldsymbol{\zeta}_1(x), \tag{19}$$

$$u_2(y,t) = \boldsymbol{a}_2^\top(t)\boldsymbol{\chi}_2(y), \quad w_2(y,t) = \boldsymbol{b}_2^\top(t)\boldsymbol{\zeta}_2(y). \tag{20}$$

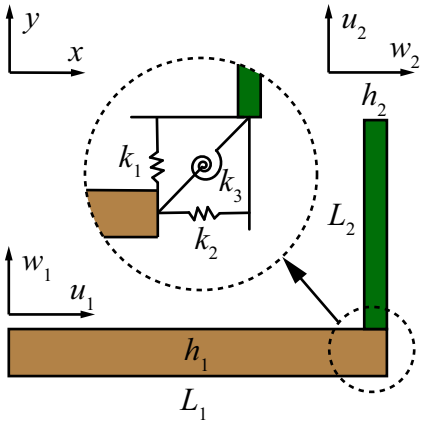

Figure 8: Geometrical model for beams connected at right angles. At the junction the artificial stiffness k_1 and k_2 are responsible for the displacements while k_3 relates to rotation. Again artificial springs are applied at the connected boundaries of each beam while global boundary conditions (zero external force and moment) are imposed on the non-connected ends of the beams. As opposed to Fig. 1, in this case the axial vibrations are taken into account. Here u_1 and w_1 respectively represent the axial and bending displacements for Beam 1, while u_2 and w_2 are those of Beam 2.

To recover the modes of Beam 1, we start computing its kinetic energy,

$$
\begin{aligned}
E_{\text{kin1}} &= \frac{1}{2}\int_0^{L_1} \rho h_1(\dot{u}_1^2 + \dot{w}_1^2)\mathrm{d}x \\
&= \frac{1}{2}\begin{bmatrix} \dot{\boldsymbol{a}}_1 \\ \dot{\boldsymbol{b}}_1 \end{bmatrix}^\top \left[\begin{array}{c|c} \int_0^{L_1} \rho h_1 \left(\boldsymbol{\chi}_1 \boldsymbol{\chi}_1^\top\right) \mathrm{d}x & \mathbf{0} \\ \hline \mathbf{0} & \int_0^{L_1} \rho h_1 \left(\boldsymbol{\zeta}_1 \boldsymbol{\zeta}_1^\top\right) \mathrm{d}x \end{array}\right] \begin{bmatrix} \dot{\boldsymbol{a}}_1 \\ \dot{\boldsymbol{b}}_1 \end{bmatrix} \\
&\equiv \frac{1}{2}\begin{bmatrix} \dot{\boldsymbol{a}}_1 \\ \dot{\boldsymbol{b}}_1 \end{bmatrix}^\top \left[\begin{array}{c|c} \boldsymbol{M}_{u1} & \mathbf{0} \\ \hline \mathbf{0} & \boldsymbol{M}_{w1} \end{array}\right] \begin{bmatrix} \dot{\boldsymbol{a}}_1 \\ \dot{\boldsymbol{b}}_1 \end{bmatrix} \\
&\equiv \frac{1}{2}\dot{\boldsymbol{c}}_1^\top \boldsymbol{M}_1 \dot{\boldsymbol{c}}_1,
\end{aligned} \tag{21}
$$

and the potential one,

$$
\begin{aligned}
E_{\text{pot1}} &= \frac{1}{2}\int_0^{L_1} Eh_1 \left(\partial_x u_1\right)^2 + EI_1 \left(\partial_{xx}^2 w_1\right)^2 \mathrm{d}x \\
&= \frac{1}{2}\begin{bmatrix} \boldsymbol{a}_1 \\ \boldsymbol{b}_1 \end{bmatrix}^\top \left[\begin{array}{c|c} \int_0^{L_1} Eh_1 \left(\partial_x \boldsymbol{\chi}_1 \partial_x \boldsymbol{\chi}_1^\top\right) \mathrm{d}x & \mathbf{0} \\ \hline \mathbf{0} & \int_0^{L_1} EI_1 \left(\partial_{xx}^2 \boldsymbol{\zeta}_1 \partial_{xx}^2 \boldsymbol{\zeta}_1^\top\right) \mathrm{d}x \end{array}\right] \begin{bmatrix} \boldsymbol{a}_1 \\ \boldsymbol{b}_1 \end{bmatrix} \\
&\equiv \frac{1}{2}\begin{bmatrix} \boldsymbol{a}_1 \\ \boldsymbol{b}_1 \end{bmatrix}^\top \left[\begin{array}{c|c} \boldsymbol{K}_{u1} & \mathbf{0} \\ \hline \mathbf{0} & \boldsymbol{K}_{w1} \end{array}\right] \begin{bmatrix} \boldsymbol{a}_1 \\ \boldsymbol{b}_1 \end{bmatrix} \\
&\equiv \frac{1}{2}\boldsymbol{c}_1^\top \boldsymbol{K}_1 \boldsymbol{c}_1.
\end{aligned} \tag{22}
$$

After building the Lagrangian we get the equations of motion,

$$
\left(\boldsymbol{K}_1 - \omega_1^2 \boldsymbol{M}_1\right) \hat{\boldsymbol{C}}_1 = \mathbf{0}, \tag{23}
$$

from which we can obtain the normalized eigen-matrix, $\overline{\boldsymbol{P}}_1 = [\overline{\boldsymbol{C}}_{1,1}, \overline{\boldsymbol{C}}_{1,2}, \overline{\boldsymbol{C}}_{1,3}, ..., \overline{\boldsymbol{C}}_{1,m}]$ of Beam 1.

We proceed equally for Beam 2 which yields,

$$
\begin{aligned}
E_{\text{kin2}} &= \frac{1}{2}\int_0^{L_2} \rho h_2(\dot{u}_2^2 + \dot{w}_2^2)\mathrm{d}y \\
&= \frac{1}{2}\begin{bmatrix} \dot{\boldsymbol{a}}_2 \\ \dot{\boldsymbol{b}}_2 \end{bmatrix}^\top \begin{bmatrix} \int_0^{L_2} \rho h_2 \left(\boldsymbol{\chi}_2 \boldsymbol{\chi}_2^\top\right) \mathrm{d}y & \mathbf{0} \\ \mathbf{0} & \int_0^{L_2} \rho h_2 \left(\boldsymbol{\zeta}_2 \boldsymbol{\zeta}_2^\top\right) \mathrm{d}y \end{bmatrix} \begin{bmatrix} \dot{\boldsymbol{a}}_2 \\ \dot{\boldsymbol{b}}_2 \end{bmatrix} \\
&\equiv \frac{1}{2}\dot{\boldsymbol{c}}_2^\top \boldsymbol{M}_2 \dot{\boldsymbol{c}}_2,
\end{aligned} \tag{24}
$$

and

$$
\begin{aligned}
E_{\text{pot2}} &= \frac{1}{2}\int_0^{L_2} Eh_2 \left(\partial_y u_2\right)^2 + EI_2 \left(\partial_{yy}^2 w_2\right)^2 \mathrm{d}y \\
&= \frac{1}{2}\begin{bmatrix} \boldsymbol{a}_2 \\ \boldsymbol{b}_2 \end{bmatrix}^\top \begin{bmatrix} \int_0^{L_2} Eh_2 \left(\partial_y \boldsymbol{\chi}_2 \partial_y \boldsymbol{\chi}_2^\top\right) \mathrm{d}y & \mathbf{0} \\ \mathbf{0} & \int_0^{L_2} EI_2 \left(\partial_{yy}^2 \boldsymbol{\zeta}_2 \partial_{yy}^2 \boldsymbol{\zeta}_2^\top\right) \mathrm{d}y \end{bmatrix} \begin{bmatrix} \boldsymbol{a}_2 \\ \boldsymbol{b}_2 \end{bmatrix} \\
&\equiv \frac{1}{2}\boldsymbol{c}_2^\top \boldsymbol{K}_2 \boldsymbol{c}_2,
\end{aligned} \tag{25}
$$

from which we derive the equations of motion,

$$
\left(\boldsymbol{K}_2 - \omega_2^2 \boldsymbol{M}_2\right)\hat{\boldsymbol{C}}_2 = \mathbf{0}. \tag{26}
$$

Solving Eq. (26) we compute the normalized eigen-matrix, $\overline{\boldsymbol{P}}_2 = [\overline{\boldsymbol{C}}_{2,1}, \overline{\boldsymbol{C}}_{2,2}, \overline{\boldsymbol{C}}_{2,3}, ..., \overline{\boldsymbol{C}}_{2,m}]$.

Next, we project the weight coefficient vectors into the modal space, i.e.,

$$
\boldsymbol{c}_1 = \overline{\boldsymbol{P}}_1 \boldsymbol{\varepsilon}_1, \quad \boldsymbol{c}_2 = \overline{\boldsymbol{P}}_2 \boldsymbol{\varepsilon}_2, \tag{27}
$$

which allows one to calculate the total kinetic energy of Beams 1 and 2 as,

$$
\begin{aligned}
E_{\text{kin}} &= E_{\text{kin1}} + E_{\text{kin2}} \\
&= \frac{1}{2}\dot{\boldsymbol{c}}_1^{\top}\boldsymbol{M}_1\dot{\boldsymbol{c}}_1 + \frac{1}{2}\dot{\boldsymbol{c}}_2^{\top}\boldsymbol{M}_2\dot{\boldsymbol{c}}_2 \\
&= \frac{1}{2}\begin{bmatrix} \dot{\boldsymbol{c}}_1 \\ \dot{\boldsymbol{c}}_2 \end{bmatrix}^{\top}\begin{bmatrix} \boldsymbol{M}_1 & \boldsymbol{0} \\ \boldsymbol{0} & \boldsymbol{M}_2 \end{bmatrix}\begin{bmatrix} \dot{\boldsymbol{c}}_1 \\ \dot{\boldsymbol{c}}_2 \end{bmatrix} \\
&= \frac{1}{2}\begin{bmatrix} \overline{\boldsymbol{P}}_1\dot{\boldsymbol{\varepsilon}}_1 \\ \overline{\boldsymbol{P}}_2\dot{\boldsymbol{\varepsilon}}_2 \end{bmatrix}^{\top}\begin{bmatrix} \boldsymbol{M}_1 & \boldsymbol{0} \\ \boldsymbol{0} & \boldsymbol{M}_2 \end{bmatrix}\begin{bmatrix} \overline{\boldsymbol{P}}_1\dot{\boldsymbol{\varepsilon}}_1 \\ \overline{\boldsymbol{P}}_2\dot{\boldsymbol{\varepsilon}}_2 \end{bmatrix} \\
&= \frac{1}{2}\begin{bmatrix} \dot{\boldsymbol{\varepsilon}}_1 \\ \dot{\boldsymbol{\varepsilon}}_2 \end{bmatrix}^{\top}\left(\begin{bmatrix} \overline{\boldsymbol{P}}_1 & \boldsymbol{0} \\ \boldsymbol{0} & \overline{\boldsymbol{P}}_2 \end{bmatrix}^{\top}\begin{bmatrix} \boldsymbol{M}_1 & \boldsymbol{0} \\ \boldsymbol{0} & \boldsymbol{M}_2 \end{bmatrix}\begin{bmatrix} \overline{\boldsymbol{P}}_1 & \boldsymbol{0} \\ \boldsymbol{0} & \overline{\boldsymbol{P}}_2 \end{bmatrix}\right)\begin{bmatrix} \dot{\boldsymbol{\varepsilon}}_1 \\ \dot{\boldsymbol{\varepsilon}}_2 \end{bmatrix} \\
&\equiv \frac{1}{2}\begin{bmatrix} \dot{\boldsymbol{\varepsilon}}_1 \\ \dot{\boldsymbol{\varepsilon}}_2 \end{bmatrix}^{\top}\begin{bmatrix} \overline{\boldsymbol{M}}_1 & \boldsymbol{0} \\ \boldsymbol{0} & \overline{\boldsymbol{M}}_2 \end{bmatrix}\begin{bmatrix} \dot{\boldsymbol{\varepsilon}}_1 \\ \dot{\boldsymbol{\varepsilon}}_2 \end{bmatrix} \\
&\equiv \frac{1}{2}\dot{\boldsymbol{\varepsilon}}^{\top}\overline{\boldsymbol{M}}\dot{\boldsymbol{\varepsilon}},
\end{aligned}
\tag{28}
$$

where $\overline{\boldsymbol{M}}_1$ and $\overline{\boldsymbol{M}}_2$ are the reduced (and normalized) mass matrices of Beam 1 and Beam 2, respectively.

The total potential energy is expressed as,

$$
\begin{aligned}
E_{\text{pot}} &= E_{\text{pot1}} + E_{\text{pot2}} \\
&= \frac{1}{2}\boldsymbol{c}_1^\top \boldsymbol{K}_1 \boldsymbol{c}_1 + \frac{1}{2}\boldsymbol{c}_2^\top \boldsymbol{K}_2 \boldsymbol{c}_2 \\
&= \frac{1}{2}\begin{bmatrix} \boldsymbol{c}_1 \\ \boldsymbol{c}_2 \end{bmatrix}^\top \begin{bmatrix} \boldsymbol{K}_1 & \boldsymbol{0} \\ \boldsymbol{0} & \boldsymbol{K}_2 \end{bmatrix} \begin{bmatrix} \boldsymbol{c}_1 \\ \boldsymbol{c}_2 \end{bmatrix} \\
&= \frac{1}{2}\begin{bmatrix} \overline{\boldsymbol{P}}_1\boldsymbol{\varepsilon}_1 \\ \overline{\boldsymbol{P}}_2\boldsymbol{\varepsilon}_2 \end{bmatrix}^\top \begin{bmatrix} \boldsymbol{K}_1 & \boldsymbol{0} \\ \boldsymbol{0} & \boldsymbol{K}_2 \end{bmatrix} \begin{bmatrix} \overline{\boldsymbol{P}}_1\boldsymbol{\varepsilon}_1 \\ \overline{\boldsymbol{P}}_2\boldsymbol{\varepsilon}_2 \end{bmatrix} \\
&= \frac{1}{2}\begin{bmatrix} \boldsymbol{\varepsilon}_1 \\ \boldsymbol{\varepsilon}_2 \end{bmatrix}^\top \left(\begin{bmatrix} \overline{\boldsymbol{P}}_1 & \boldsymbol{0} \\ \boldsymbol{0} & \overline{\boldsymbol{P}}_2 \end{bmatrix}^\top \begin{bmatrix} \boldsymbol{K}_1 & \boldsymbol{0} \\ \boldsymbol{0} & \boldsymbol{K}_2 \end{bmatrix} \begin{bmatrix} \overline{\boldsymbol{P}}_1 & \boldsymbol{0} \\ \boldsymbol{0} & \overline{\boldsymbol{P}}_2 \end{bmatrix} \right) \begin{bmatrix} \boldsymbol{\varepsilon}_1 \\ \boldsymbol{\varepsilon}_2 \end{bmatrix} \\
&\equiv \frac{1}{2}\begin{bmatrix} \boldsymbol{\varepsilon}_1 \\ \boldsymbol{\varepsilon}_2 \end{bmatrix}^\top \begin{bmatrix} \overline{\boldsymbol{K}}_1 & \boldsymbol{0} \\ \boldsymbol{0} & \overline{\boldsymbol{K}}_2 \end{bmatrix} \begin{bmatrix} \boldsymbol{\varepsilon}_1 \\ \boldsymbol{\varepsilon}_2 \end{bmatrix} \\
&\equiv \frac{1}{2}\boldsymbol{\varepsilon}^\top \overline{\boldsymbol{K}}\boldsymbol{\varepsilon},
\end{aligned} \tag{29}
$$

where $\overline{\boldsymbol{K}}_1$ and $\overline{\boldsymbol{K}}_2$ are the reduced stiffness matrices of Beams 1 and 2.

Next, we must couple the reduced-order models of the two individual beams. The coupling conditions to be satisfied at the joint between Beam 1 and Beam 2 in the current case are

$$
\begin{aligned}
\lim_{k_1 \to +\infty} w_1(L_1) - u_2(0) &= 0, \\
\lim_{k_2 \to +\infty} u_1(L_1) - w_2(0) &= 0, \\
\lim_{k_3 \to +\infty} \partial_x w_1(L_1) - \partial_y w_2(0) &= 0.
\end{aligned} \tag{30}
$$

Knowing that, we can derive the potential energy stored at the two artificial translational springs and at

the rotational one (see Fig. 8). For the first translational spring we get,

$$
\begin{aligned}
E_{\mathrm{spr1}} =& \frac{1}{2} k_1 [w_1(L_1) - u_2(0)]^2 \\
=& \frac{1}{2} k_1 [w_1^2(L_1) - w_1(L_1)u_2(0) - u_2(0)w_1(L_1) + u_2^2(0)] \\
=& \frac{1}{2} k_1 [\boldsymbol{b}_1^\top \boldsymbol{\zeta}_1(L_1)\boldsymbol{\zeta}_1^\top(L_1)\boldsymbol{b}_1 - \boldsymbol{b}_1^\top \boldsymbol{\zeta}_1(L_1)\boldsymbol{\chi}_2^\top(0)\boldsymbol{a}_2 - \boldsymbol{a}_2^\top \boldsymbol{\chi}_2(0)\boldsymbol{\zeta}_1^\top(L_1)\boldsymbol{b}_1 + \boldsymbol{a}_2^\top \boldsymbol{\chi}_2(0)\boldsymbol{\chi}_2^\top(0)\boldsymbol{a}_2] \\
=& \frac{1}{2} \begin{bmatrix} \boldsymbol{b}_1 \\ \boldsymbol{a}_2 \end{bmatrix}^\top \left[\begin{array}{c|c} k_1\boldsymbol{\zeta}_1(L_1)\boldsymbol{\zeta}_1^\top(L_1) & -k_1\boldsymbol{\zeta}_1(L_1)\boldsymbol{\chi}_2^\top(0) \\ \hline -k_1\boldsymbol{\chi}_2(0)\boldsymbol{\zeta}_1^\top(L_1) & k_1\boldsymbol{\chi}_2(0)\boldsymbol{\chi}_2^\top(0) \end{array}\right] \begin{bmatrix} \boldsymbol{b}_1 \\ \boldsymbol{a}_2 \end{bmatrix} \\
\equiv& \frac{1}{2} \begin{bmatrix} \boldsymbol{b}_1 \\ \boldsymbol{a}_2 \end{bmatrix}^\top \left[\begin{array}{c|c} \boldsymbol{K}_{\mathrm{sp1},11} & -\boldsymbol{K}_{\mathrm{sp1},12} \\ \hline -\boldsymbol{K}_{\mathrm{sp1},12}^\top & \boldsymbol{K}_{\mathrm{sp1},22} \end{array}\right] \begin{bmatrix} \boldsymbol{b}_1 \\ \boldsymbol{a}_2 \end{bmatrix},
\end{aligned} \tag{31}
$$

and for the second one,

$$
\begin{aligned}
E_{\mathrm{spr2}} =& \frac{1}{2} k_2 [u_1(L_1) - w_2(0)]^2 \\
=& \frac{1}{2} \begin{bmatrix} \boldsymbol{a}_1 \\ \boldsymbol{b}_2 \end{bmatrix}^\top \left[\begin{array}{c|c} k_2\boldsymbol{\chi}_1(L_1)\boldsymbol{\chi}_1^\top(L_1) & -k_2\boldsymbol{\chi}_1(L_1)\boldsymbol{\zeta}_2^\top(0) \\ \hline -k_2\boldsymbol{\zeta}_2(0)\boldsymbol{\chi}_1^\top(L_1) & k_2\boldsymbol{\zeta}_2(0)\boldsymbol{\zeta}_2^\top(0) \end{array}\right] \begin{bmatrix} \boldsymbol{a}_1 \\ \boldsymbol{b}_2 \end{bmatrix} \\
\equiv& \frac{1}{2} \begin{bmatrix} \boldsymbol{a}_1 \\ \boldsymbol{b}_2 \end{bmatrix}^\top \left[\begin{array}{c|c} \boldsymbol{K}_{\mathrm{sp2},11} & -\boldsymbol{K}_{\mathrm{sp2},12} \\ \hline -\boldsymbol{K}_{\mathrm{sp2},12}^\top & \boldsymbol{K}_{\mathrm{sp2},22} \end{array}\right] \begin{bmatrix} \boldsymbol{a}_1 \\ \boldsymbol{b}_2 \end{bmatrix}.
\end{aligned} \tag{32}
$$

In the case of the rotational spring, the stored energy becomes

$$
\begin{aligned}
E_{\mathrm{spr3}} =& \frac{1}{2} k_3 [\partial_x w_1(L_1) - \partial_y w_2(0)]^2 \\
=& \frac{1}{2} \begin{bmatrix} \boldsymbol{b}_1 \\ \boldsymbol{b}_2 \end{bmatrix}^\top \left[\begin{array}{c|c} k_3 \partial_x \boldsymbol{\zeta}_1(L_1) \partial_x \boldsymbol{\zeta}_1^\top(L_1) & -k_3 \partial_x \boldsymbol{\zeta}_1(L_1) \partial_y \boldsymbol{\zeta}_2^\top(0) \\ \hline -k_3 \partial_y \boldsymbol{\zeta}_2(0) \partial_x \boldsymbol{\zeta}_1^\top(L_1) & k_3 \partial_y \boldsymbol{\zeta}_2(0) \partial_y \boldsymbol{\zeta}_2^\top(0) \end{array}\right] \begin{bmatrix} \boldsymbol{b}_1 \\ \boldsymbol{b}_2 \end{bmatrix} \\
\equiv& \frac{1}{2} \begin{bmatrix} \boldsymbol{b}_1 \\ \boldsymbol{b}_2 \end{bmatrix}^\top \left[\begin{array}{c|c} \boldsymbol{K}_{\mathrm{sp3},11} & -\boldsymbol{K}_{\mathrm{sp3},12} \\ \hline -\boldsymbol{K}_{\mathrm{sp3},12}^\top & \boldsymbol{K}_{\mathrm{sp3},22} \end{array}\right] \begin{bmatrix} \boldsymbol{b}_1 \\ \boldsymbol{b}_2 \end{bmatrix}.
\end{aligned} \tag{33}
$$

Therefore, the total potential energy of the artificial springs reads in compact form

$$
\begin{aligned}
E_{\mathrm{spr}} &= E_{\mathrm{spr1}} + E_{\mathrm{spr2}} + E_{\mathrm{spr3}} \\
&= \frac{1}{2} \begin{bmatrix} \boldsymbol{a}_1 \\ \boldsymbol{b}_1 \\ \boldsymbol{a}_2 \\ \boldsymbol{b}_2 \end{bmatrix}^\top \begin{bmatrix} \boldsymbol{K}_{\mathrm{sp2},11} & \boldsymbol{0} & \boldsymbol{0} & -\boldsymbol{K}_{\mathrm{sp2},12} \\ \boldsymbol{0} & \boldsymbol{K}_{\mathrm{sp1},11} + \boldsymbol{K}_{\mathrm{sp3},11} & -\boldsymbol{K}_{\mathrm{sp1},12} & -\boldsymbol{K}_{\mathrm{sp3},12} \\ \boldsymbol{0} & -\boldsymbol{K}_{\mathrm{sp1},12}^\top & \boldsymbol{K}_{\mathrm{sp1},22} & \boldsymbol{0} \\ -\boldsymbol{K}_{\mathrm{sp1},12}^\top & -\boldsymbol{K}_{\mathrm{sp3},12}^\top & \boldsymbol{0} & \boldsymbol{K}_{\mathrm{sp2},22} + \boldsymbol{K}_{\mathrm{sp3},22} \end{bmatrix} \begin{bmatrix} \boldsymbol{a}_1 \\ \boldsymbol{b}_1 \\ \boldsymbol{a}_2 \\ \boldsymbol{b}_2 \end{bmatrix} \\
&\equiv \frac{1}{2} \begin{bmatrix} \boldsymbol{c}_1 \\ \boldsymbol{c}_2 \end{bmatrix}^\top \boldsymbol{K}_{\mathrm{coup}} \begin{bmatrix} \boldsymbol{c}_1 \\ \boldsymbol{c}_2 \end{bmatrix} \\
&= \frac{1}{2} \begin{bmatrix} \boldsymbol{\varepsilon}_1 \\ \boldsymbol{\varepsilon}_2 \end{bmatrix}^\top \left(\begin{bmatrix} \overline{\boldsymbol{P}}_1 & \boldsymbol{0} \\ \boldsymbol{0} & \overline{\boldsymbol{P}}_2 \end{bmatrix}^\top \boldsymbol{K}_{\mathrm{coup}} \begin{bmatrix} \overline{\boldsymbol{P}}_1 & \boldsymbol{0} \\ \boldsymbol{0} & \overline{\boldsymbol{P}}_2 \end{bmatrix} \right) \begin{bmatrix} \boldsymbol{\varepsilon}_1 \\ \boldsymbol{\varepsilon}_2 \end{bmatrix} \\
&\equiv \frac{1}{2} \boldsymbol{\varepsilon}^\top \overline{\boldsymbol{K}}_{\mathrm{coup}} \boldsymbol{\varepsilon}.
\end{aligned} \tag{34}
$$

Applying the Euler-Lagrangian equations to $\mathscr{L} = E_{\mathrm{kin}} - E_{\mathrm{pot}} - E_{\mathrm{spr}}$ we arrive at the reduced-order eigenvalue problem,

$$
\left(\overline{\boldsymbol{K}} + \overline{\boldsymbol{K}}_{\mathrm{coup}} - \omega^2 \overline{\boldsymbol{M}}\right) \hat{\boldsymbol{\varepsilon}} = \boldsymbol{0}, \tag{35}
$$

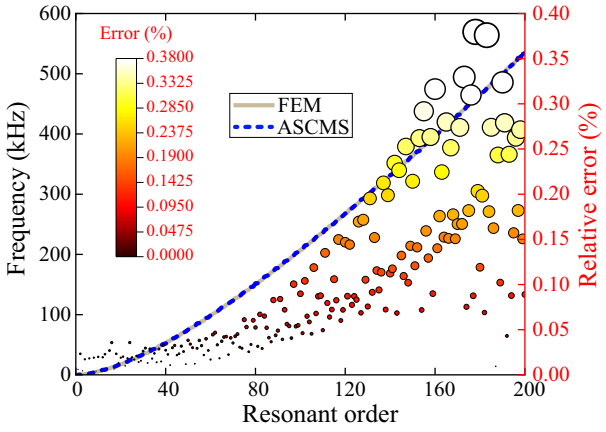

Figure 9: Comparison of modal frequencies computed with the ASCMS (blue dash line) and FEM (brown solid line) for the two beams connected at right angles. To better appreciate their differences, the relative error $|f_{\text{ASCMS}} - f_{\text{FEM}}|/f_{\text{FEM}} \times 100\%$ has been calculated and shown in red at the right y axis. For the ease of exposition, the relative error at each resonant order is represented by a circle whose radius and colour are proportional to the relative error value.

which is analogous to Eq. (18) but for the two beams connected at right angles.

4.1.2. Numerical results

The geometries and materials of the two beams considered hereafter are the same as those in the tests of section 3. For the simulations we take $\alpha = 2$ and $\beta = 200$. To validate the ASCMS for the current example, in Fig. 9 we have plotted the modal frequencies corresponding to the first 200 modal orders of the coupled two-beam system computed with both, the ASCMS based on GEM (blue dashed line) and the FEM (brown line). As can be seen, the ASCMS result is very close to that of the FEM, i.e., the blue dashed line is almost indistinguishable from the brown solid line. To reflect the slight differences between these two curves, in

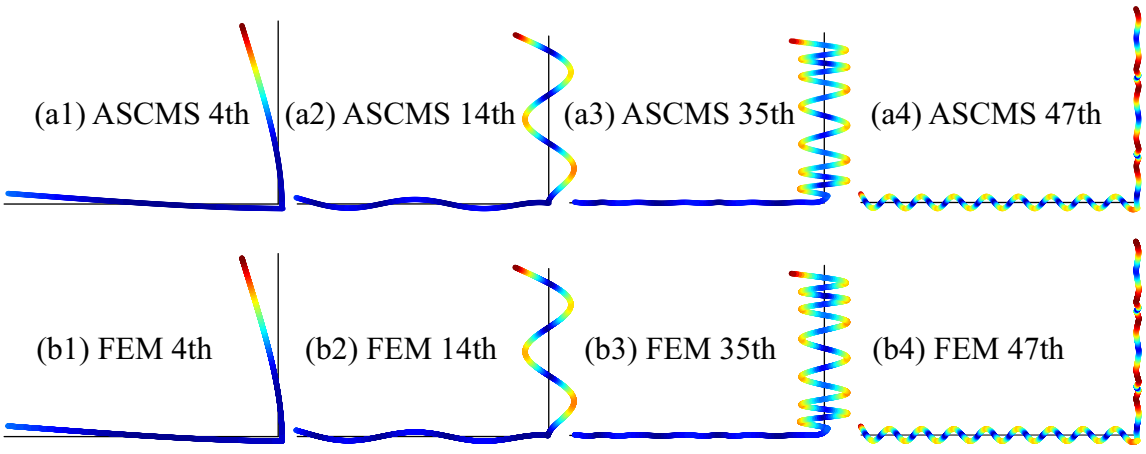

Figure 10: Comparison of the 4-th, 14-th, 35-th, and 47-th modal shapes obtained from ASCMS (top row) and FEM (bottom row). The black lines represent the beams before deformation, while the coloured shapes show the displacements $||u_i||^2 + ||w_i||^2,\ i = 1, 2.$

the figure we have also plotted the relative error between the ASCMS and FEM frequency values for each resonant order, computed as $\epsilon_{100\%} = |f_{\text{ASCMS}} - f_{\text{FEM}}|/f_{\text{FEM}} \times 100\%$. The range of variation of $\epsilon_{100\%}$ is indicated in the right axis of Fig. 9 (red colour). To facilitate the inspection of the value of $\epsilon_{100\%}$ for each resonant order, we have drawn a circle for each whose radius and colour are proportional to $\epsilon_{100\%}$. It can be observed that for the lower orders (< 100) the relative error is smaller than 0.1%. As one could expect, the error increases with the resonant order, but the maximum value does not exceed 0.38%, which confirms the high degree of accuracy of the ASCMS method. Furthermore, some arbitrary modal shapes obtained from ASCMS simulations have been plotted in Fig. 10 and compared to FEM ones. Again, the resemblance between the results of the two methods is very significant. It is also observed in the figure how in-plane vibrations strongly couple with bending ones. Likewise, let us mention that the computational time without modal truncation is 1.156 s, while for the reduced model (with $\alpha = 2$) becomes 0.354 s.

4.2. Application 2: A cylindrical shell with an internal floor partition

Let us now turn to the more complex case of a cylindrical shell coupled to a flat interior partition (see Fig. 11). As already mentioned, this type of structures can be found in simplified models of aircraft and submarines. Note that for this problem it will be necessary to consider displacements in all three directions (vertical, axial and longitudinal). We will start by presenting the synthesis of the model and then show the results and again the validation by comparison with a finite element model.

4.2.1. Synthesis procedure

We begin with by expanding the displacement fields in the vertical, w, axial, v, and longitudinal, u, directions (see Fig. 11) in terms of approximating functions,

$$u_{\text{s}}(x,y,t) = \boldsymbol{a}_{\text{s}}^{\top}(t)\boldsymbol{\chi}_{\text{s}}(x,y), \quad v_{\text{s}}(x,y,t) = \boldsymbol{b}_{\text{s}}^{\top}(t)\boldsymbol{\gamma}_{\text{s}}(x,y), \quad w_{\text{s}}(x,y,t) = \boldsymbol{c}_{\text{s}}^{\top}(t)\boldsymbol{\zeta}_{\text{s}}(x,y), \tag{36}$$

$$u_{\text{p}}(x,y,t) = \boldsymbol{a}_{\text{p}}^{\top}(t)\boldsymbol{\chi}_{\text{p}}(x,y), \quad v_{\text{p}}(x,y,t) = \boldsymbol{b}_{\text{p}}^{\top}(t)\boldsymbol{\gamma}_{\text{p}}(x,y), \quad w_{\text{p}}(x,y,t) = \boldsymbol{c}_{\text{p}}^{\top}(t)\boldsymbol{\zeta}_{\text{p}}(x,y), \tag{37}$$

where the subscripts s and p respectively represent variables corresponding to the shell and the plate. The kinetic energy of the cylindrical shell is given by,

$$
\begin{aligned}
E_{\mathrm{kin,s}} &= \frac{1}{2}\int_{-\pi R}^{\pi R}\int_{0}^{L_x} \rho h_{\mathrm{s}}\left(\dot{u}_{\mathrm{s}}^2+\dot{v}_{\mathrm{s}}^2+\dot{w}_{\mathrm{s}}^2\right)\mathrm{d}x\mathrm{d}y \\
&\equiv \frac{1}{2}\begin{bmatrix}\dot{\boldsymbol{a}}_{\mathrm{s}}\\ \dot{\boldsymbol{b}}_{\mathrm{s}}\\ \dot{\boldsymbol{c}}_{\mathrm{s}}\end{bmatrix}^{\top}\begin{bmatrix}\boldsymbol{M}_{\mathrm{us}} & \boldsymbol{0} & \boldsymbol{0}\\ \boldsymbol{0} & \boldsymbol{M}_{\mathrm{vs}} & \boldsymbol{0}\\ \boldsymbol{0} & \boldsymbol{0} & \boldsymbol{M}_{\mathrm{ws}}\end{bmatrix}\begin{bmatrix}\dot{\boldsymbol{a}}_{\mathrm{s}}\\ \dot{\boldsymbol{b}}_{\mathrm{s}}\\ \dot{\boldsymbol{c}}_{\mathrm{s}}\end{bmatrix} \\
&\equiv \frac{1}{2}\dot{\boldsymbol{d}}_{\mathrm{s}}^{\top}\boldsymbol{M}_{\mathrm{s}}\dot{\boldsymbol{d}}_{\mathrm{s}},
\end{aligned}
\tag{38}
$$

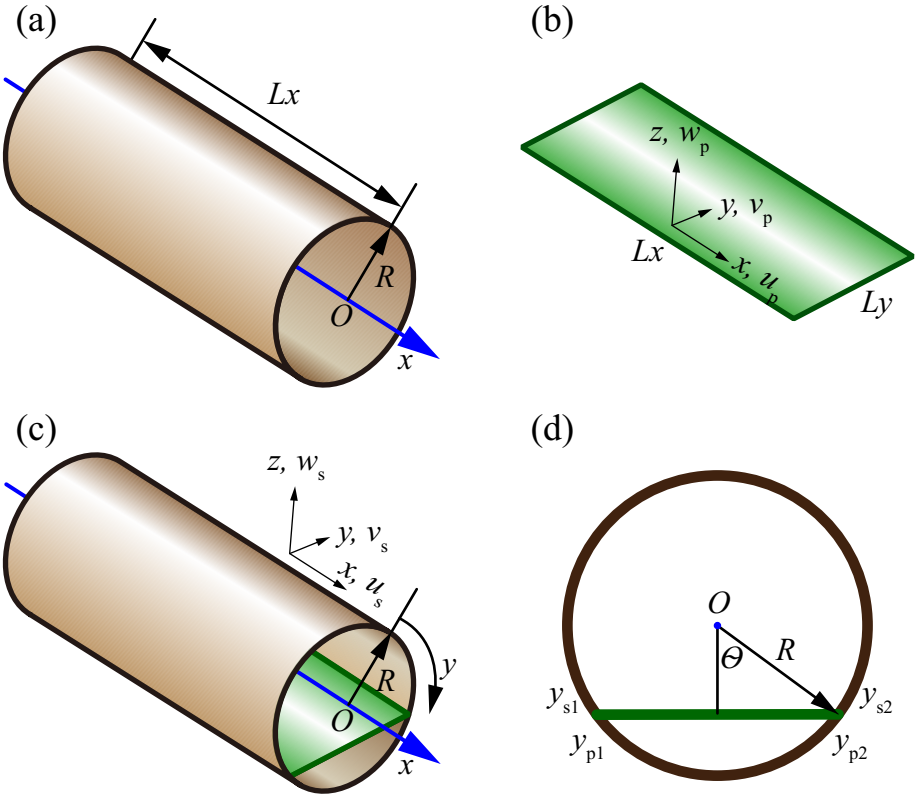

Figure 11: Illustration of (a) a standard cylindrical shell, (b) a rectangular plate, (c)-(d) the coupled built-up structure in 3D and front views, respectively. The in-plane displacements of the plate are denoted by u_{p} and v_{p}, while w_{p} stands for the bending one. As for the cylindrical shell, u_{s}, v_{s}, and w_{s} respectively represent the axial, circumferential, and radial displacements. The plate location is characterized by angle θ, as seen in (d).

and the potential one by,

$$
\begin{aligned}
E_{\mathrm{pot,s}} =& \frac{1}{2}\int_{-\pi R}^{\pi R}\int_{0}^{L_x} D_{\mathrm{s}}\left[\left(\partial_{xx}^2 w_{\mathrm{s}}\right)^2+\left(\partial_{yy}^2 w_{\mathrm{s}}-\frac{1}{R}\partial_y v_{\mathrm{s}}\right)^2\right.\\
&\left.+2\nu\partial_{xx}^2 w_{\mathrm{s}}\left(\partial_{yy}^2 w_{\mathrm{s}}-\frac{1}{R}\partial_y v_{\mathrm{s}}\right)+\frac{1-\nu}{2}\left(2\partial_{xy}^2 w_{\mathrm{s}}-\frac{2}{R}\partial_x v_{\mathrm{s}}\right)^2\right]\mathrm{d}x\mathrm{d}y\\
&+\frac{1}{2}\int_{-\pi R}^{\pi R}\int_{0}^{L_x} G_{\mathrm{s}}\left[\left(\partial_x u_{\mathrm{s}}\right)^2+\left(\partial_y v_{\mathrm{s}}+\frac{w_{\mathrm{s}}}{R}\right)^2\right.\\
&\left.+2\nu\partial_x u_{\mathrm{s}}\left(\partial_y v_{\mathrm{s}}+\frac{w_{\mathrm{s}}}{R}\right)+\frac{1-\nu}{2}\left(\partial_x v_{\mathrm{s}}+\partial_y u_{\mathrm{s}}\right)^2\right]\mathrm{d}x\mathrm{d}y\\
\equiv&\frac{1}{2}\begin{bmatrix}\boldsymbol{a}_{\mathrm{s}}\\ \boldsymbol{b}_{\mathrm{s}}\\ \boldsymbol{c}_{\mathrm{s}}\end{bmatrix}^{\top}\begin{bmatrix}\boldsymbol{K}_{\mathrm{usus}} & \boldsymbol{K}_{\mathrm{usvs}} & \boldsymbol{K}_{\mathrm{usws}}\\ \boldsymbol{K}_{\mathrm{usvs}}^{\top} & \boldsymbol{K}_{\mathrm{vsvs}} & \boldsymbol{K}_{\mathrm{vsws}}\\ \boldsymbol{K}_{\mathrm{usws}}^{\top} & \boldsymbol{K}_{\mathrm{vsws}}^{\top} & \boldsymbol{K}_{\mathrm{wsws}}\end{bmatrix}\begin{bmatrix}\boldsymbol{a}_{\mathrm{s}}\\ \boldsymbol{b}_{\mathrm{s}}\\ \boldsymbol{c}_{\mathrm{s}}\end{bmatrix}\\
\equiv&\frac{1}{2}\boldsymbol{d}_{\mathrm{s}}^{\top}\boldsymbol{K}_{\mathrm{s}}\boldsymbol{d}_{\mathrm{s}},
\end{aligned}
\tag{39}
$$

where $D_{\mathrm{s}}=\frac{Eh_{\mathrm{s}}^3}{12(1-\nu^2)}$ is the bending stiffness and $G_{\mathrm{s}}=\frac{Eh_{\mathrm{s}}}{1-\nu^2}$ the extensional one. For the sake of brevity, the stiffness matrices in Eq. (39) are not listed herein. The interested reader can find them e.g., in [41]. Building the Lagrangian from Eqs. (38) and (39) we obtain the equations of motion for the shell,

$$
\left(\boldsymbol{K}_{\mathrm{s}}-\omega_{\mathrm{s}}^2\boldsymbol{M}_{\mathrm{s}}\right)\hat{\boldsymbol{D}}_{\mathrm{s}}=\boldsymbol{0},
\tag{40}
$$

and solving Eq. (40) we find the shell resonances and eigenvectors. We can select the first m ones and get the reduced eigen-matrix, $\overline{\boldsymbol{P}}_{\mathrm{s}}=[\overline{\boldsymbol{D}}_{\mathrm{s},1},\overline{\boldsymbol{D}}_{\mathrm{s},2},\overline{\boldsymbol{D}}_{\mathrm{s},3},...,\overline{\boldsymbol{D}}_{\mathrm{s},m}]$.

Likewise, the kinetic and potential energies of the plate read

$$
\begin{aligned}
E_{\mathrm{kin,p}} &= \frac{1}{2}\int_{0}^{L_y}\int_{0}^{L_x}\rho h_{\mathrm{p}}\left(\dot{u}_{\mathrm{p}}^2+\dot{v}_{\mathrm{p}}^2+\dot{w}_{\mathrm{p}}^2\right)\mathrm{d}x\mathrm{d}y\\
&\equiv\frac{1}{2}\begin{bmatrix}\dot{\boldsymbol{a}}_{\mathrm{p}}\\ \dot{\boldsymbol{b}}_{\mathrm{p}}\\ \dot{\boldsymbol{c}}_{\mathrm{p}}\end{bmatrix}^{\top}\begin{bmatrix}\boldsymbol{M}_{\mathrm{up}} & \boldsymbol{0} & \boldsymbol{0}\\ \boldsymbol{0} & \boldsymbol{M}_{\mathrm{vp}} & \boldsymbol{0}\\ \boldsymbol{0} & \boldsymbol{0} & \boldsymbol{M}_{\mathrm{wp}}\end{bmatrix}\begin{bmatrix}\dot{\boldsymbol{a}}_{\mathrm{p}}\\ \dot{\boldsymbol{b}}_{\mathrm{p}}\\ \dot{\boldsymbol{c}}_{\mathrm{p}}\end{bmatrix}\\
&\equiv\frac{1}{2}\dot{\boldsymbol{d}}_{\mathrm{p}}^{\top}\boldsymbol{M}_{\mathrm{p}}\dot{\boldsymbol{d}}_{\mathrm{p}},
\end{aligned}
\tag{41}
$$

and

$$
\begin{aligned}
E_{\mathrm{pot,p}} =& \frac{1}{2}\int_0^{L_y}\int_0^{L_x} D_{\mathrm{p}}\left[\left(\partial_{xx}^2 w_{\mathrm{p}}\right)^2+\left(\partial_{yy}^2 w_{\mathrm{p}}\right)^2\right. \\
&\left.+2\nu\partial_{xx}^2 w_{\mathrm{p}}\partial_{yy}^2 w_{\mathrm{p}}+\frac{1-\nu}{2}\left(2\partial_{xy}^2 w_{\mathrm{p}}\right)^2\right]\mathrm{d}x\mathrm{d}y \\
&+\frac{1}{2}\int_0^{L_y}\int_0^{L_x} G_{\mathrm{p}}\left[\left(\partial_x u_{\mathrm{p}}\right)^2+\left(\partial_y v_{\mathrm{p}}\right)^2\right. \\
&\left.+2\nu\partial_x u_{\mathrm{p}}\partial_y v_{\mathrm{p}}+\frac{1-\nu}{2}\left(\partial_x v_{\mathrm{p}}+\partial_y u_{\mathrm{p}}\right)^2\right]\mathrm{d}x\mathrm{d}y \\
\equiv& \frac{1}{2}\begin{bmatrix}\boldsymbol{a}_{\mathrm{p}}\\ \boldsymbol{b}_{\mathrm{p}}\\ \boldsymbol{c}_{\mathrm{p}}\end{bmatrix}^{\top}\begin{bmatrix}\boldsymbol{K}_{\mathrm{upup}} & \boldsymbol{K}_{\mathrm{upvp}} & \boldsymbol{0}\\ \boldsymbol{K}_{\mathrm{upvp}}^{\top} & \boldsymbol{K}_{\mathrm{vpvp}} & \boldsymbol{0}\\ \boldsymbol{0} & \boldsymbol{0} & \boldsymbol{K}_{\mathrm{wpwp}}\end{bmatrix}\begin{bmatrix}\boldsymbol{a}_{\mathrm{p}}\\ \boldsymbol{b}_{\mathrm{p}}\\ \boldsymbol{c}_{\mathrm{p}}\end{bmatrix} \\
\equiv& \frac{1}{2}\boldsymbol{d}_{\mathrm{p}}^{\top}\boldsymbol{K}_{\mathrm{p}}\boldsymbol{d}_{\mathrm{p}},
\end{aligned}
\tag{42}
$$

from which we obtain the equations of motion for the plate,

$$
\left(\boldsymbol{K}_{\mathrm{p}}-\omega_{\mathrm{p}}^2\boldsymbol{M}_{\mathrm{p}}\right)\hat{\boldsymbol{D}}_{\mathrm{p}}=\boldsymbol{0}. \tag{43}
$$

The solution to Eq. (43) provides the eigenvectors of the plate and choosing m of them, we get the reduced eigen-matrix, $\overline{\boldsymbol{P}}_{\mathrm{p}}=[\overline{\boldsymbol{D}}_{\mathrm{p},1},\overline{\boldsymbol{D}}_{\mathrm{p},2},\overline{\boldsymbol{D}}_{\mathrm{p},3},...,\overline{\boldsymbol{D}}_{\mathrm{p},m}]$

As done for the beam examples, we next project the weight coefficient vectors to the modal space,

$$
\begin{aligned}
\boldsymbol{d}_{\mathrm{s}} &= \overline{\boldsymbol{P}}_{\mathrm{s}}\boldsymbol{\varepsilon}_{\mathrm{s}},\\
\boldsymbol{d}_{\mathrm{p}} &= \overline{\boldsymbol{P}}_{\mathrm{p}}\boldsymbol{\varepsilon}_{\mathrm{p}},
\end{aligned}
\tag{44}
$$

where $\boldsymbol{\varepsilon}_{\mathrm{s}}$ and $\boldsymbol{\varepsilon}_{\mathrm{p}}$ designate the vectors of modal participation factors.

The kinetic energy of the built-up system (cylindrical shell plus inner plate) becomes,

$$
\begin{aligned}
E_{\text{kin,total}} &= E_{\text{kins}} + E_{\text{kinp}} \\
&= \frac{1}{2}\dot{\boldsymbol{d}}_{\text{s}}^{\top}\boldsymbol{M}_{\text{s}}\dot{\boldsymbol{d}}_{\text{s}} + \frac{1}{2}\dot{\boldsymbol{d}}_{\text{p}}^{\top}\boldsymbol{M}_{\text{p}}\dot{\boldsymbol{d}}_{\text{p}} \\
&= \frac{1}{2}\begin{bmatrix} \dot{\boldsymbol{\varepsilon}}_{\text{s}} \\ \dot{\boldsymbol{\varepsilon}}_{\text{p}} \end{bmatrix}^{\top}\left(\begin{bmatrix} \overline{\boldsymbol{P}}_{\text{s}} & \boldsymbol{0} \\ \boldsymbol{0} & \overline{\boldsymbol{P}}_{\text{p}} \end{bmatrix}^{\top}\begin{bmatrix} \boldsymbol{M}_{\text{s}} & \boldsymbol{0} \\ \boldsymbol{0} & \boldsymbol{M}_{\text{p}} \end{bmatrix}\begin{bmatrix} \overline{\boldsymbol{P}}_{\text{s}} & \boldsymbol{0} \\ \boldsymbol{0} & \overline{\boldsymbol{P}}_{\text{p}} \end{bmatrix}\right)\begin{bmatrix} \dot{\boldsymbol{\varepsilon}}_{\text{s}} \\ \dot{\boldsymbol{\varepsilon}}_{\text{p}} \end{bmatrix} \\
&\equiv \frac{1}{2}\dot{\boldsymbol{\varepsilon}}^{\top}\overline{\boldsymbol{M}}\dot{\boldsymbol{\varepsilon}},
\end{aligned}
\tag{45}
$$

where $\overline{\boldsymbol{M}}_{\text{s}}$ and $\overline{\boldsymbol{M}}_{\text{p}}$ are the reduced mass matrices of the shell and the plate, respectively. For the potential energy we get

$$
\begin{aligned}
E_{\text{pot,total}} &= E_{\text{pot,s}} + E_{\text{pot,p}} \\
&= \frac{1}{2}\boldsymbol{d}_{\text{s}}^{\top}\boldsymbol{K}_{\text{s}}\boldsymbol{d}_{\text{s}} + \frac{1}{2}\boldsymbol{d}_{\text{p}}^{\top}\boldsymbol{K}_{\text{p}}\boldsymbol{c}_{\text{p}} \\
&= \frac{1}{2}\begin{bmatrix} \boldsymbol{\varepsilon}_{\text{s}} \\ \boldsymbol{\varepsilon}_{\text{p}} \end{bmatrix}^{\top}\left(\begin{bmatrix} \overline{\boldsymbol{P}}_{\text{s}} & \boldsymbol{0} \\ \boldsymbol{0} & \overline{\boldsymbol{P}}_{\text{p}} \end{bmatrix}^{\top}\begin{bmatrix} \boldsymbol{K}_{\text{s}} & \boldsymbol{0} \\ \boldsymbol{0} & \boldsymbol{K}_{\text{p}} \end{bmatrix}\begin{bmatrix} \overline{\boldsymbol{P}}_{\text{s}} & \boldsymbol{0} \\ \boldsymbol{0} & \overline{\boldsymbol{P}}_{\text{p}} \end{bmatrix}\right)\begin{bmatrix} \boldsymbol{\varepsilon}_{\text{s}} \\ \boldsymbol{\varepsilon}_{\text{p}} \end{bmatrix} \\
&\equiv \frac{1}{2}\boldsymbol{\varepsilon}^{\top}\overline{\boldsymbol{K}}\boldsymbol{\varepsilon}.
\end{aligned}
\tag{46}
$$

The next step is to consider the energy contribution from the artificial springs linking the plate and the shell. The coupling conditions at the junction between both substructures are expressed as (Figs. 11 c and 11d),

$$
\begin{aligned}
&\lim_{k_1\to+\infty} v_{\text{s}}(y_{\text{s1}})\sin\theta + w_{\text{s}}(y_{\text{s1}})\cos\theta - w_{\text{p}}(y_{\text{p1}}) = 0, \qquad \lim_{k_1\to+\infty} -v_{\text{s}}(y_{\text{s2}})\sin\theta + w_{\text{s}}(y_{\text{s2}})\cos\theta - w_{\text{p}}(y_{\text{p2}}) = 0, \\
&\lim_{k_2\to+\infty} v_{\text{s}}(y_{\text{s1}})\cos\theta - w_{\text{s}}(y_{\text{s1}})\sin\theta - v_{\text{p}}(y_{\text{p1}}) = 0, \qquad \lim_{k_2\to+\infty} v_{\text{s}}(y_{\text{s2}})\cos\theta + w_{\text{s}}(y_{\text{s2}})\sin\theta - v_{\text{p}}(y_{\text{p2}}) = 0, \\
&\lim_{k_3\to+\infty} -\frac{v_{\text{s}}(y_{\text{s1}})}{R} + \partial_y w_{\text{s}}(y_{\text{s1}}) - \partial_y w_{\text{p}}(y_{\text{p1}}) = 0, \qquad \lim_{k_3\to+\infty} -\frac{v_{\text{s}}(y_{\text{s2}})}{R} + \partial_y w_{\text{s}}(y_{\text{s2}}) - \partial_y w_{\text{p}}(y_{\text{p2}}) = 0, \\
&\lim_{k_4\to+\infty} u_{\text{s}}(y_{\text{s1}}) - u_{\text{p}}(y_{\text{p1}}) = 0, \qquad \lim_{k_4\to+\infty} u_{\text{s}}(y_{\text{s2}}) - u_{\text{p}}(y_{\text{p2}}) = 0.
\end{aligned}
\tag{47}
$$

The above conditions allows us to calculate the energy stored at the artificial springs. For k_1, we have from

the first line in Eq. (47),

$$
\begin{aligned}
E_{\mathrm{spr1}} =& \frac{1}{2} k_1 \int_0^{L_1} [v_{\mathrm{s}}(y_{\mathrm{s1}}) \sin\theta + w_{\mathrm{s}}(y_{\mathrm{s1}}) \cos\theta - w_{\mathrm{p}}(y_{\mathrm{p1}})]^2 \mathrm{d}x \\
&+ \frac{1}{2} k_1 \int_0^{L_1} [-v_{\mathrm{s}}(y_{\mathrm{s2}}) \sin\theta + w_{\mathrm{s}}(y_{\mathrm{s2}}) \cos\theta - w_{\mathrm{p}}(y_{\mathrm{p2}})]^2 \mathrm{d}x \\
\equiv& \frac{1}{2} \begin{bmatrix} \boldsymbol{b}_{\mathrm{s}} \\ \boldsymbol{c}_{\mathrm{s}} \\ \boldsymbol{c}_{\mathrm{p}} \end{bmatrix}^{\top} \begin{bmatrix} \boldsymbol{K}_{\mathrm{spr1,vsvs}} & \boldsymbol{K}_{\mathrm{spr1,vsws}} & \boldsymbol{K}_{\mathrm{spr1,vswp}} \\ \boldsymbol{K}_{\mathrm{spr1,vsws}}^{\top} & \boldsymbol{K}_{\mathrm{spr1,wsws}} & \boldsymbol{K}_{\mathrm{spr1,wswp}} \\ \boldsymbol{K}_{\mathrm{spr1,vswp}}^{\top} & \boldsymbol{K}_{\mathrm{spr1,wswp}}^{\top} & \boldsymbol{K}_{\mathrm{spr1,wpwp}} \end{bmatrix} \begin{bmatrix} \boldsymbol{b}_{\mathrm{s}} \\ \boldsymbol{c}_{\mathrm{s}} \\ \boldsymbol{c}_{\mathrm{p}} \end{bmatrix} \\
\equiv& \frac{1}{2} \begin{bmatrix} \boldsymbol{b}_{\mathrm{s}} \\ \boldsymbol{c}_{\mathrm{s}} \\ \boldsymbol{c}_{\mathrm{p}} \end{bmatrix}^{\top} \boldsymbol{K}_{\mathrm{spr1}} \begin{bmatrix} \boldsymbol{b}_{\mathrm{s}} \\ \boldsymbol{c}_{\mathrm{s}} \\ \boldsymbol{c}_{\mathrm{p}} \end{bmatrix},
\end{aligned} \tag{48}
$$

while for k_2 and the second line in Eq. (47),

$$
\begin{aligned}
E_{\mathrm{spr2}} =& \frac{1}{2} k_2 \int_0^{L_1} [v_{\mathrm{s}}(y_{\mathrm{s1}}) \cos\theta - w_{\mathrm{s}}(y_{\mathrm{s1}}) \sin\theta - v_{\mathrm{p}}(y_{\mathrm{p1}})]^2 \mathrm{d}x \\
&+ \frac{1}{2} k_2 \int_0^{L_1} [v_{\mathrm{s}}(y_{\mathrm{s2}}) \cos\theta + w_{\mathrm{s}}(y_{\mathrm{s2}}) \sin\theta - v_{\mathrm{p}}(y_{\mathrm{p2}})]^2 \mathrm{d}x \\
\equiv& \frac{1}{2} \begin{bmatrix} \boldsymbol{b}_{\mathrm{s}} \\ \boldsymbol{c}_{\mathrm{s}} \\ \boldsymbol{b}_{\mathrm{p}} \end{bmatrix}^{\top} \begin{bmatrix} \boldsymbol{K}_{\mathrm{spr2,vsvs}} & \boldsymbol{K}_{\mathrm{spr2,vsws}} & \boldsymbol{K}_{\mathrm{spr2,vsvp}} \\ \boldsymbol{K}_{\mathrm{spr2,vsws}}^{\top} & \boldsymbol{K}_{\mathrm{spr2,wsws}} & \boldsymbol{K}_{\mathrm{spr2,wsvp}} \\ \boldsymbol{K}_{\mathrm{spr2,vsvp}}^{\top} & \boldsymbol{K}_{\mathrm{spr2,wsvp}}^{\top} & \boldsymbol{K}_{\mathrm{spr2,vpvp}} \end{bmatrix} \begin{bmatrix} \boldsymbol{b}_{\mathrm{s}} \\ \boldsymbol{c}_{\mathrm{s}} \\ \boldsymbol{b}_{\mathrm{p}} \end{bmatrix} \\
\equiv& \frac{1}{2} \begin{bmatrix} \boldsymbol{b}_{\mathrm{s}} \\ \boldsymbol{c}_{\mathrm{s}} \\ \boldsymbol{b}_{\mathrm{p}} \end{bmatrix}^{\top} \boldsymbol{K}_{\mathrm{spr2}} \begin{bmatrix} \boldsymbol{b}_{\mathrm{s}} \\ \boldsymbol{c}_{\mathrm{s}} \\ \boldsymbol{b}_{\mathrm{p}} \end{bmatrix}.
\end{aligned} \tag{49}
$$

The energy stored in the third and fourth type of artificial connection springs (constraints in the third and

fourth lines in Eq. (47)) respectively becomes,

$$
\begin{aligned}
E_{\mathrm{spr3}} =& \frac{1}{2}k_3\int_0^{L_1}\left[-\frac{v_{\mathrm{s}}(y_{\mathrm{s1}})}{R}+\partial_y w_{\mathrm{s}}(y_{\mathrm{s1}})-\partial_y w_{\mathrm{p}}(y_{\mathrm{p1}})\right]^2\mathrm{d}x \\
&+\frac{1}{2}k_3\int_0^{L_1}\left[-\frac{v_{\mathrm{s}}(y_{\mathrm{s2}})}{R}+\partial_y w_{\mathrm{s}}(y_{\mathrm{s2}})-\partial_y w_{\mathrm{p}}(y_{\mathrm{p2}})\right]^2\mathrm{d}x \\
\equiv& \frac{1}{2}\begin{bmatrix}\boldsymbol{b}_{\mathrm{s}}\\ \boldsymbol{c}_{\mathrm{s}}\\ \boldsymbol{c}_{\mathrm{p}}\end{bmatrix}^{\top}\begin{bmatrix}\boldsymbol{K}_{\mathrm{spr3,vsvs}} & \boldsymbol{K}_{\mathrm{spr3,vsws}} & \boldsymbol{K}_{\mathrm{spr3,vswp}}\\ \boldsymbol{K}_{\mathrm{spr3,vsws}}^{\top} & \boldsymbol{K}_{\mathrm{spr3,wsws}} & \boldsymbol{K}_{\mathrm{spr3,wswp}}\\ \boldsymbol{K}_{\mathrm{spr3,vswp}}^{\top} & \boldsymbol{K}_{\mathrm{spr3,wswp}}^{\top} & \boldsymbol{K}_{\mathrm{spr3,wpwp}}\end{bmatrix}\begin{bmatrix}\boldsymbol{b}_{\mathrm{s}}\\ \boldsymbol{c}_{\mathrm{s}}\\ \boldsymbol{c}_{\mathrm{p}}\end{bmatrix} \\
\equiv& \frac{1}{2}\begin{bmatrix}\boldsymbol{b}_{\mathrm{s}}\\ \boldsymbol{c}_{\mathrm{s}}\\ \boldsymbol{c}_{\mathrm{p}}\end{bmatrix}^{\top}\boldsymbol{K}_{\mathrm{spr3}}\begin{bmatrix}\boldsymbol{b}_{\mathrm{s}}\\ \boldsymbol{c}_{\mathrm{s}}\\ \boldsymbol{c}_{\mathrm{p}}\end{bmatrix},
\end{aligned}
\tag{50}
$$

and

$$
\begin{aligned}
E_{\mathrm{spr4}} =& \frac{1}{2}k_4\int_0^{L_1}[u_{\mathrm{s}}(y_{\mathrm{s1}})-u_{\mathrm{p}}(y_{\mathrm{p1}})]^2\mathrm{d}x+\frac{1}{2}k_4\int_0^{L_1}[u_{\mathrm{s}}(y_{\mathrm{s2}})-u_{\mathrm{p}}(y_{\mathrm{p2}})]^2\mathrm{d}x \\
\equiv& \frac{1}{2}\begin{bmatrix}\boldsymbol{a}_{\mathrm{s}}\\ \boldsymbol{a}_{\mathrm{p}}\end{bmatrix}^{\top}\begin{bmatrix}\boldsymbol{K}_{\mathrm{spr4,usus}} & \boldsymbol{K}_{\mathrm{spr4,usup}}\\ \boldsymbol{K}_{\mathrm{spr4,usup}}^{\top} & \boldsymbol{K}_{\mathrm{spr4,upup}}\end{bmatrix}\begin{bmatrix}\boldsymbol{a}_{\mathrm{s}}\\ \boldsymbol{a}_{\mathrm{p}}\end{bmatrix} \\
\equiv& \frac{1}{2}\begin{bmatrix}\boldsymbol{a}_{\mathrm{s}}\\ \boldsymbol{a}_{\mathrm{p}}\end{bmatrix}^{\top}\boldsymbol{K}_{\mathrm{spr4}}\begin{bmatrix}\boldsymbol{a}_{\mathrm{s}}\\ \boldsymbol{a}_{\mathrm{p}}\end{bmatrix}.
\end{aligned}
\tag{51}
$$

The entries of $\boldsymbol{K}_{\mathrm{spr}i}$ $(i=1,2,3,4)$ in Eqs. (48)-(51) are provided in Appendix B.

The total potential energy stored in the artificial springs can be written in more compact form as

$$
\begin{aligned}
E_{\mathrm{pot,total}} &= E_{\mathrm{spr1}} + E_{\mathrm{spr2}} + E_{\mathrm{spr3}} + E_{\mathrm{spr4}} \\
&= \frac{1}{2}\begin{bmatrix} \boldsymbol{a}_\mathrm{s} \\ \boldsymbol{b}_\mathrm{s} \\ \boldsymbol{c}_\mathrm{s} \\ \boldsymbol{a}_\mathrm{p} \\ \boldsymbol{b}_\mathrm{p} \\ \boldsymbol{c}_\mathrm{p} \end{bmatrix}^\top \begin{bmatrix} \boldsymbol{K}_\mathrm{usus} & \boldsymbol{0} & \boldsymbol{0} & \boldsymbol{K}_\mathrm{usup} & \boldsymbol{0} & \boldsymbol{0} \\ \boldsymbol{0} & \boldsymbol{K}_\mathrm{vsvs} & \boldsymbol{K}_\mathrm{vsws} & \boldsymbol{0} & \boldsymbol{K}_\mathrm{vsvp} & \boldsymbol{K}_\mathrm{vswp} \\ \boldsymbol{0} & \boldsymbol{K}_\mathrm{vsws}^\top & \boldsymbol{K}_\mathrm{wsws} & \boldsymbol{0} & \boldsymbol{K}_\mathrm{wsvp} & \boldsymbol{K}_\mathrm{wswp} \\ \boldsymbol{K}_\mathrm{usup}^\top & \boldsymbol{0} & \boldsymbol{0} & \boldsymbol{K}_\mathrm{upup} & \boldsymbol{0} & \boldsymbol{0} \\ \boldsymbol{0} & \boldsymbol{K}_\mathrm{vsvp}^\top & \boldsymbol{K}_\mathrm{wsvp}^\top & \boldsymbol{0} & \boldsymbol{K}_\mathrm{vpvp} & \boldsymbol{0} \\ \boldsymbol{0} & \boldsymbol{K}_\mathrm{vswp}^\top & \boldsymbol{K}_\mathrm{wswp}^\top & \boldsymbol{0} & \boldsymbol{0} & \boldsymbol{K}_\mathrm{wpwp} \end{bmatrix} \begin{bmatrix} \boldsymbol{a}_\mathrm{s} \\ \boldsymbol{b}_\mathrm{s} \\ \boldsymbol{c}_\mathrm{s} \\ \boldsymbol{a}_\mathrm{p} \\ \boldsymbol{b}_\mathrm{p} \\ \boldsymbol{c}_\mathrm{p} \end{bmatrix} \\
&\equiv \frac{1}{2}\begin{bmatrix} \boldsymbol{d}_\mathrm{s} \\ \boldsymbol{d}_\mathrm{p} \end{bmatrix}^\top \boldsymbol{K}_\mathrm{coup} \begin{bmatrix} \boldsymbol{d}_\mathrm{s} \\ \boldsymbol{d}_\mathrm{p} \end{bmatrix} \\
&= \frac{1}{2}\begin{bmatrix} \boldsymbol{\varepsilon}_\mathrm{s} \\ \boldsymbol{\varepsilon}_\mathrm{p} \end{bmatrix}^\top \left(\begin{bmatrix} \overline{\boldsymbol{P}}_1 & \boldsymbol{0} \\ \boldsymbol{0} & \overline{\boldsymbol{P}}_2 \end{bmatrix}^\top \boldsymbol{K}_\mathrm{coup} \begin{bmatrix} \overline{\boldsymbol{P}}_1 & \boldsymbol{0} \\ \boldsymbol{0} & \overline{\boldsymbol{P}}_2 \end{bmatrix} \right) \begin{bmatrix} \boldsymbol{\varepsilon}_\mathrm{s} \\ \boldsymbol{\varepsilon}_\mathrm{p} \end{bmatrix} \\
&\equiv \frac{1}{2}\boldsymbol{\varepsilon}^\top \overline{\boldsymbol{K}}_\mathrm{coup} \boldsymbol{\varepsilon}.
\end{aligned} \tag{52}
$$

The elements of $\boldsymbol{K}_\mathrm{coup}$ are provided in Appendix C.

From Eqs. (45), (46) and (52) we construct the Lagrangian of the built-up system and from the Euler-Lagrange equations we finally arrive at the reduced-order eigenvalue problem,

$$
\left(\overline{\boldsymbol{K}} + \overline{\boldsymbol{K}}_\mathrm{coup} - \omega^2 \overline{\boldsymbol{M}}\right) \hat{\boldsymbol{\varepsilon}} = \boldsymbol{0}. \tag{53}
$$

4.2.2. Numerical results

To validate the ASCMS method using GEM for the cylindrical shell plus inner plate model we proceed as for the two-beam at right angles example, and perform comparisons with FEM simulations. We consider both substructures to be made of steel. The shell has radius $R = 1$ m, length $L_x = 5$ m and thickness $h_\mathrm{s} = 0.02$ m, while the plate at $\cos(\theta) = 0.5$ has the same length and thickness. The FEM model has been built with the commercial code Comsol Multiphysics using the *Shell* module. To ensure convergence up to

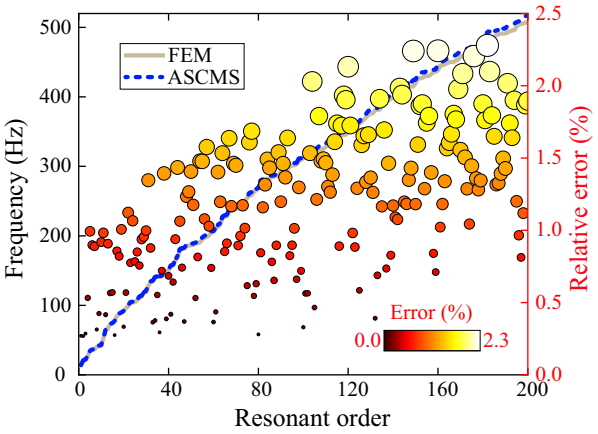

Figure 12: Comparison of modal frequencies computed with the ASCMS (blue dash line) and FEM (brown solid line) for the cylindrical shell connected to an inner floor. To observe the differences, the relative error $|f_{\text{ASCMS}} - f_{\text{FEM}}|/f_{\text{FEM}} \times 100\%$ has been calculated for the range shown in the red, right y axis of the figure. For the ease of exposition, the relative error at each resonant order is represented with circles whose radii and colours are proportional to the relative error values.

520 Hz (see Fig. 12), which corresponds to a bending wavelength of $\lambda = 0.616$ m, the standard criteria of taking a mesh size of $h = \lambda/10$ has been chosen. The FEM mesh of the coupled model consists of a total of 11508 quadratic Lagrange quadrilateral elements, with 11560 nodes and 278850 dofs.

Fig. 12 is the analogous to Fig. 9 but for the current cylindrical shell plus inner plate coupled system. The figure shows the modal frequencies for each resonant order calculated with the ASCMS (dashed blue line) and with the FEM (continuous brown line). Again, both lines are almost indistinguishable except for the highest modes. Even for this more complex example the degree of accuracy of the ASCMS is remarkable. As observed in the figure, the relative error values for each resonant mode, $\epsilon_{100\%}$ (represented by circles) does not surpass 2.3%. The resemblance between the ASCMS results and the FEM ones is also confirmed when looking at the mode shapes exhibited in Fig. 13 (which is analogous to Fig. 10 in the previous example). In particular, we can observe that, both the global modes (as the 105-th one) and the local modes (as the 135-th one involving the plate and the 162-nd one involving the shell) are well reproduced by the ASCMS. On the other hand, it only cost 44.8 seconds to get the solution considering the reduced model with $n_{\text{p}} = 1215$ modes for the plate and $n_{\text{s}} = 2673$ modes for the shell, while it took 468.5 s for the full original model. This confirms the ASCMS as a reliable approach to build modal reduced-order models of built-up systems and simulate the vibrational behaviour of complex structures.

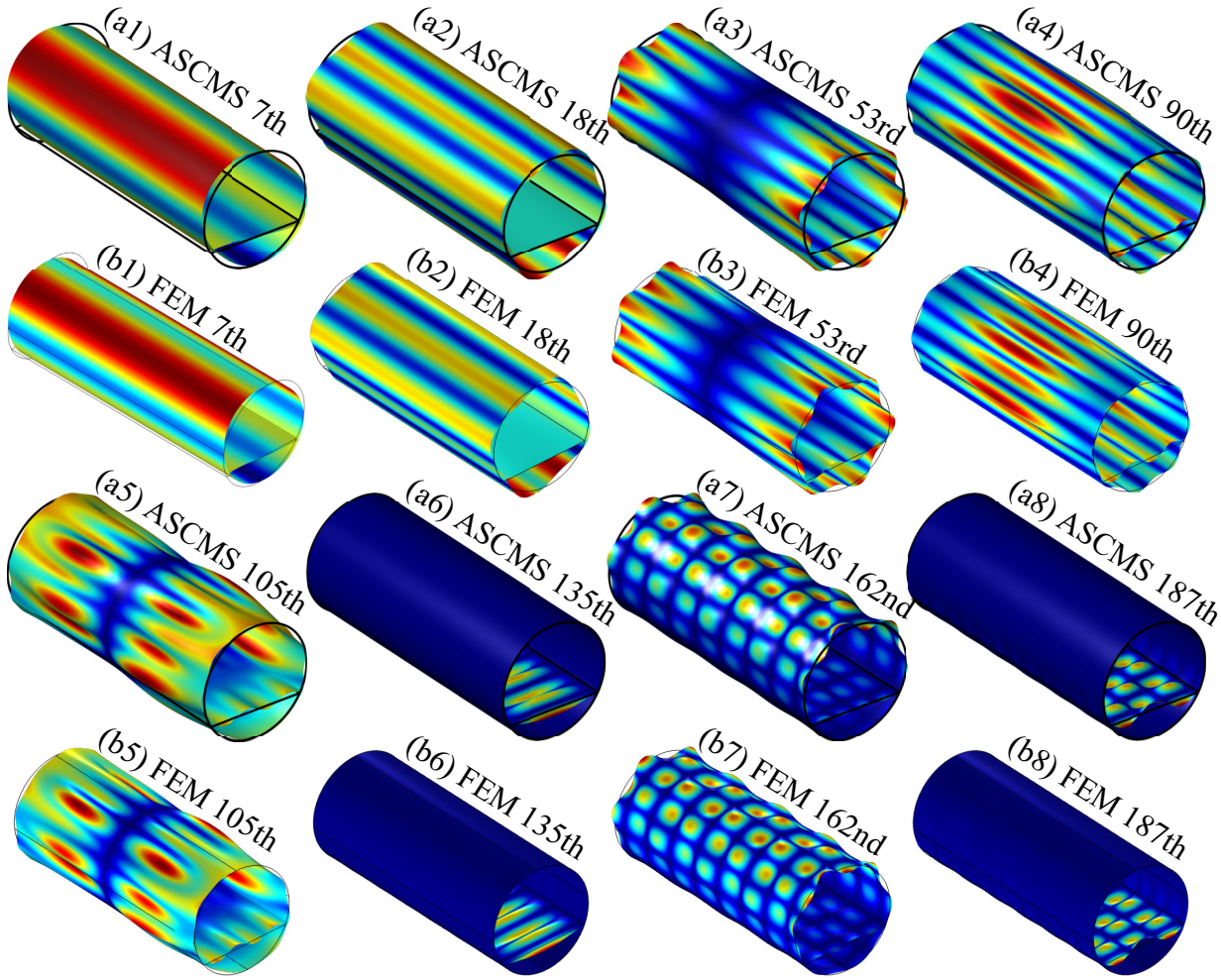

Figure 13: Comparison of the 7-th, 18-th, 53-rd, 90-th, 105-th, 135-th, 162-nd and 187-th modal shapes obtained from (a1)-(a8) ASCMS and (b1)-(b8) FEM. The black lines stand for the shell and the plate before deformation, while the coloured shapes show the displacements $||u_i||^2 + ||v_i||^2 + ||w_i||^2,\ i = p, s$.

5. Conclusions

In this paper, we have developed an artificial spring component mode synthesis (ASCMS) method to characterize the vibrational behaviour of built-up systems composed of various substructures. As opposed to the traditional artificial spring method that expands the displacement fields in the space domain, the ASCMS relies on the modal information of each substructure. This allows one to obtain the stiffness coupling matrix accounting for the artificial springs in the modal space and to construct a modal reduced-order model of the total system based on the modes of each substructure. The artificial spring method has therefore been combined with component mode synthesis (CMS) approaches in the ASCMS.

For ease of exposition, the ASCMS theory was initially presented for two beams connected in the axial direction. This example has been used to study the convergence of the method as a function of several factors. First, the influence of the stiffness values of the artificial springs has been analyzed. A simple procedure has been provided to choose the stiffness value that guarantees convergence up to a selected eigenfrequency of the built-up structure. Then, the influence of the coupling force has been inspected by coupling beams of different thickness ratio. The ASCMS has yielded accurate results in all cases, showing that the method can be applied with confidence for very different coupling forces. Finally, modal truncation has been examined in terms of modal participation factors, showing that almost all resonant orders exceeding the target eigenfrequency of the fully coupled system can be discarded.

After validation of the ASCMS theory for a simple case, more complex examples have been addressed. The first consisted of two beams connected at right angles for which the in-plane motion must be considered in addition to the bending motion. The second is more industrial and has consisted of an inner floor connected to a cylindrical shell, a structure typically found in aeronautical and naval applications. For this case, displacements in the vertical, axial and longitudinal directions have been taken into account. It has been shown that ASCMS easily adapts to these more complex situations and comparison with FEM models has revealed a high degree of accuracy. It should be mentioned that system damping has not been included in the examples presented, although this could easily be taken into account by considering a complex stiffness matrix whose imaginary part accounts for system losses. This will not imply any substantial change in the ASCMS methodology.

Finally, it should be mentioned that although only fully coupled substructures have been contemplated in this work, it is expected that ASCMS can also work well for elastic connections. This will be addressed in future work along with the inclusion of damping at the connection interfaces.

Acknowledgments

This work is supported by the Fundamental Research Funds for the Central Universities (Grant No. G2022KY05106), National Natural Science Foundation of China (Grant Nos. 11704314 and 52171323), and the China Postdoctoral Science Foundation (Grant No. 2018M631194).

Appendix A: Influence of the artificial spring

Let us take a simple example to see how the artificial coupling spring affects a built-up system. As shown in Fig. A1a, a resonator having mass $m = 2$ kg is connected to the ground by springs k_1 and k_2, thus

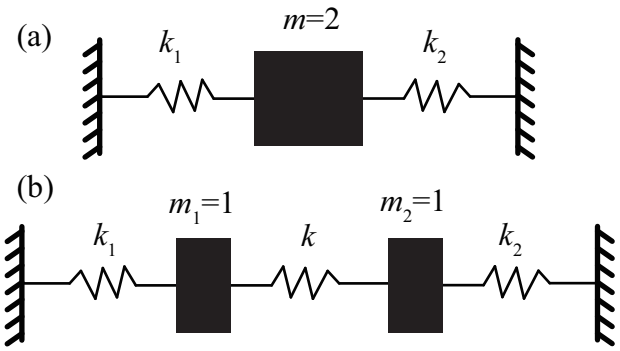

Figure A1: (a) Illustration of a resonator having two springs in parallel. (b) Illustration of dividing the resonator into two and assembling them by an artificial spring k.

the eigenvalue of the resonator is $\lambda = \frac{k_1+k_2}{2}$. Now we divide the block into two and reconnect them by an artificial spring, k, with each mass being $m_i = 1$ kg $(i = 1, 2)$ (see Fig. A1b).

Because of the simplicity of the system, we can directly obtain the equations of motion of the system in Fig. A1b,

$$\left(\begin{bmatrix} k+k_1 & -k \\ -k & k+k_2 \end{bmatrix} - \lambda \begin{bmatrix} 1 & 0 \\ 0 & 1 \end{bmatrix} \right) \begin{bmatrix} w_1 \\ w_2 \end{bmatrix} = \begin{bmatrix} 0 \\ 0 \end{bmatrix}. \tag{A1}$$

Solving Eq. A1, we obtain the eigenvalues

$$\lambda_{\mp} = \frac{k_1 + k_2 + 2k \mp \sqrt{4k^2 + (k_1 - k_2)^2}}{2}, \tag{A2}$$

It can be seen that only λ_- is acceptable because when $k \gg \frac{|k_1-k_2|}{2}$ the mode of the system in Fig. A1b converges to that of the system in Fig. A1a (i.e., $\lambda = \frac{k_1+k_2}{2}$). That is, after considering one rigid constraint, the number of degrees of freedom (dofs) of the system is reduced in one. It can be reasonably predicted that, if h constraints are imposed into two substructures respectively having n_1 and n_2 dofs, the final dofs of the built-up system become $n_1 + n_2 - h$. In particular, we can see that there is no upper limit for the value of k in λ_-. However, one must be careful when using very large k in numerical implementations, as round-off effects may deteriorate convergence.

Appendix B: Stiffness matrices for each springs

The entries of $\boldsymbol{K}_{\mathrm{spr1}}$ are:

$$\boldsymbol{K}_{\mathrm{spr1,vsvs}} = k_1 \int_0^{L_x} \boldsymbol{\gamma}_{\mathrm{s}}(x, y_{\mathrm{s1}}) \boldsymbol{\gamma}_{\mathrm{s}}^{\top}(x, y_{\mathrm{s1}}) \sin^2\theta \mathrm{d}x + k_1 \int_0^{L_x} \boldsymbol{\gamma}_{\mathrm{s}}(x, y_{\mathrm{s2}}) \boldsymbol{\gamma}_{\mathrm{s}}^{\top}(x, y_{\mathrm{s2}}) \sin^2\theta \mathrm{d}x, \tag{B1}$$

$$\boldsymbol{K}_{\mathrm{spr1,vsws}} = -k_1 \int_0^{L_x} \boldsymbol{\gamma}_{\mathrm{s}}(x, y_{\mathrm{s1}}) \boldsymbol{\zeta}_{\mathrm{s}}^{\top}(x, y_{\mathrm{s1}}) \sin\theta\cos\theta \mathrm{d}x + k_1 \int_0^{L_x} \boldsymbol{\gamma}_{\mathrm{s}}(x, y_{\mathrm{s2}}) \boldsymbol{\zeta}_{\mathrm{s}}^{\top}(x, y_{\mathrm{s2}}) \sin\theta\cos\theta \mathrm{d}x, \tag{B2}$$

$$\boldsymbol{K}_{\mathrm{spr1,vswp}} = -k_1 \int_0^{L_x} \boldsymbol{\gamma}_{\mathrm{s}}(x, y_{\mathrm{s1}}) \boldsymbol{\zeta}_{\mathrm{p}}^{\top}(x, y_{\mathrm{p1}}) \sin\theta \mathrm{d}x + k_1 \int_0^{L_x} \boldsymbol{\gamma}_{\mathrm{s}}(x, y_{\mathrm{s2}}) \boldsymbol{\zeta}_{\mathrm{p}}^{\top}(x, y_{\mathrm{p2}}) \sin\theta \mathrm{d}x, \tag{B3}$$

$$\boldsymbol{K}_{\mathrm{spr1,wsws}} = k_1 \int_0^{L_x} \boldsymbol{\zeta}_{\mathrm{s}}(x, y_{\mathrm{s1}}) \boldsymbol{\zeta}_{\mathrm{s}}^{\top}(x, y_{\mathrm{s1}}) \cos^2\theta \mathrm{d}x + k_1 \int_0^{L_x} \boldsymbol{\zeta}_{\mathrm{s}}(x, y_{\mathrm{s2}}) \boldsymbol{\zeta}_{\mathrm{s}}^{\top}(x, y_{\mathrm{s2}}) \cos^2\theta \mathrm{d}x, \tag{B4}$$

$$\boldsymbol{K}_{\mathrm{spr1,wswp}} = -k_1 \int_0^{L_x} \boldsymbol{\zeta}_{\mathrm{s}}(x, y_{\mathrm{s1}}) \boldsymbol{\zeta}_{\mathrm{p}}^{\top}(x, y_{\mathrm{p1}}) \cos\theta \mathrm{d}x - k_1 \int_0^{L_x} \boldsymbol{\zeta}_{\mathrm{s}}(x, y_{\mathrm{s2}}) \boldsymbol{\zeta}_{\mathrm{p}}^{\top}(x, y_{\mathrm{p2}}) \cos\theta \mathrm{d}x, \tag{B5}$$

$$\boldsymbol{K}_{\mathrm{spr1,wpwp}} = k_1 \int_0^{L_x} \boldsymbol{\zeta}_{\mathrm{p}}(x, y_{\mathrm{p1}}) \boldsymbol{\zeta}_{\mathrm{p}}^{\top}(x, y_{\mathrm{p1}}) \mathrm{d}x + k_1 \int_0^{L_x} \boldsymbol{\zeta}_{\mathrm{p}}(x, y_{\mathrm{p2}}) \boldsymbol{\zeta}_{\mathrm{p}}^{\top}(x, y_{\mathrm{p2}}) \mathrm{d}x. \tag{B6}$$

While the entries of $\boldsymbol{K}_{\mathrm{spr2}}$ write:

$$\boldsymbol{K}_{\mathrm{spr2,vsvs}} = k_2 \int_0^{L_x} \boldsymbol{\gamma}_{\mathrm{s}}(x, y_{\mathrm{s1}}) \boldsymbol{\gamma}_{\mathrm{s}}^{\top}(x, y_{\mathrm{s1}}) \cos^2\theta \mathrm{d}x + k_2 \int_0^{L_x} \boldsymbol{\gamma}_{\mathrm{s}}(x, y_{\mathrm{s2}}) \boldsymbol{\gamma}_{\mathrm{s}}^{\top}(x, y_{\mathrm{s2}}) \cos^2\theta \mathrm{d}x, \tag{B7}$$

$$\boldsymbol{K}_{\mathrm{spr2,vsws}} = k_2 \int_0^{L_x} \boldsymbol{\gamma}_{\mathrm{s}}(x, y_{\mathrm{s1}}) \boldsymbol{\zeta}_{\mathrm{s}}^{\top}(x, y_{\mathrm{s1}}) \sin\theta\cos\theta \mathrm{d}x - k_2 \int_0^{L_x} \boldsymbol{\gamma}_{\mathrm{s}}(x, y_{\mathrm{s2}}) \boldsymbol{\zeta}_{\mathrm{s}}^{\top}(x, y_{\mathrm{s2}}) \sin\theta\cos\theta \mathrm{d}x, \tag{B8}$$

$$\boldsymbol{K}_{\mathrm{spr2,vsvp}} = -k_2 \int_0^{L_x} \boldsymbol{\gamma}_{\mathrm{s}}(x, y_{\mathrm{s1}}) \boldsymbol{\gamma}_{\mathrm{p}}^{\top}(x, y_{\mathrm{p1}}) \cos\theta \mathrm{d}x - k_2 \int_0^{L_x} \boldsymbol{\gamma}_{\mathrm{s}}(x, y_{\mathrm{s2}}) \boldsymbol{\gamma}_{\mathrm{p}}^{\top}(x, y_{\mathrm{p2}}) \cos\theta \mathrm{d}x, \tag{B9}$$

$$\boldsymbol{K}_{\mathrm{spr2,wsws}} = k_2 \int_0^{L_x} \boldsymbol{\zeta}_{\mathrm{s}}(x, y_{\mathrm{s1}}) \boldsymbol{\zeta}_{\mathrm{s}}^{\top}(x, y_{\mathrm{s1}}) \sin^2\theta \mathrm{d}x + k_2 \int_0^{L_x} \boldsymbol{\zeta}_{\mathrm{s}}(x, y_{\mathrm{s2}}) \boldsymbol{\zeta}_{\mathrm{s}}^{\top}(x, y_{\mathrm{s2}}) \sin^2\theta \mathrm{d}x, \tag{B10}$$

$$\boldsymbol{K}_{\mathrm{spr2,wsvp}} = -k_2 \int_0^{L_x} \boldsymbol{\zeta}_{\mathrm{s}}(x, y_{\mathrm{s1}}) \boldsymbol{\gamma}_{\mathrm{p}}^{\top}(x, y_{\mathrm{p1}}) \cos\theta \mathrm{d}x - k_2 \int_0^{L_x} \boldsymbol{\zeta}_{\mathrm{s}}(x, y_{\mathrm{s2}}) \boldsymbol{\gamma}_{\mathrm{p}}^{\top}(x, y_{\mathrm{p2}}) \cos\theta \mathrm{d}x, \tag{B11}$$

$$\boldsymbol{K}_{\mathrm{spr2,vpvp}} = k_2 \int_0^{L_x} \boldsymbol{\gamma}_{\mathrm{p}}(x, y_{\mathrm{p1}}) \boldsymbol{\gamma}_{\mathrm{p}}^{\top}(x, y_{\mathrm{p1}}) \mathrm{d}x + k_2 \int_0^{L_x} \boldsymbol{\gamma}_{\mathrm{p}}(x, y_{\mathrm{p2}}) \boldsymbol{\gamma}_{\mathrm{p}}^{\top}(x, y_{\mathrm{p2}}) \mathrm{d}x. \tag{B12}$$

Whereas the entries of $\boldsymbol{K}_{\mathrm{spr3}}$ read:

$$\boldsymbol{K}_{\mathrm{spr3,vsvs}} = k_3 \int_0^{L_x} \boldsymbol{\gamma}_{\mathrm{s}}(x, y_{\mathrm{s1}}) \boldsymbol{\gamma}_{\mathrm{s}}^{\top}(x, y_{\mathrm{s1}}) \frac{1}{R^2} \mathrm{d}x + k_3 \int_0^{L_x} \boldsymbol{\gamma}_{\mathrm{s}}(x, y_{\mathrm{s2}}) \boldsymbol{\gamma}_{\mathrm{s}}^{\top}(x, y_{\mathrm{s2}}) \frac{1}{R^2} \mathrm{d}x, \tag{B13}$$

$$\boldsymbol{K}_{\mathrm{spr3,vsws}} = -k_3 \int_0^{L_x} \boldsymbol{\gamma}_{\mathrm{s}}(x, y_{\mathrm{s1}}) \partial_y \boldsymbol{\zeta}_{\mathrm{s}}^{\top}(x, y_{\mathrm{s1}}) \frac{1}{R} \mathrm{d}x - k_3 \int_0^{L_x} \boldsymbol{\gamma}_{\mathrm{s}}(x, y_{\mathrm{s2}}) \partial_y \boldsymbol{\zeta}_{\mathrm{s}}^{\top}(x, y_{\mathrm{s2}}) \frac{1}{R^2} \mathrm{d}x, \tag{B14}$$

$$\boldsymbol{K}_{\mathrm{spr3,vswp}} = k_3 \int_0^{L_x} \boldsymbol{\gamma}_{\mathrm{s}}(x, y_{\mathrm{s1}}) \partial_y \boldsymbol{\zeta}_{\mathrm{p}}^{\top}(x, y_{\mathrm{p1}}) \frac{1}{R} \mathrm{d}x + k_3 \int_0^{L_x} \boldsymbol{\gamma}_{\mathrm{s}}(x, y_{\mathrm{s2}}) \partial_y \boldsymbol{\zeta}_{\mathrm{p}}^{\top}(x, y_{\mathrm{p2}}) \frac{1}{R} \mathrm{d}x, \tag{B15}$$

$$\boldsymbol{K}_{\mathrm{spr3,wsws}} = k_3 \int_0^{L_x} \partial_y \boldsymbol{\zeta}_{\mathrm{s}}(x, y_{\mathrm{s1}}) \partial_y \boldsymbol{\zeta}_{\mathrm{s}}^{\top}(x, y_{\mathrm{s1}}) \mathrm{d}x + k_3 \int_0^{L_x} \partial_y \boldsymbol{\zeta}_{\mathrm{s}}(x, y_{\mathrm{s2}}) \partial_y \boldsymbol{\zeta}_{\mathrm{s}}^{\top}(x, y_{\mathrm{s2}}) \mathrm{d}x, \tag{B16}$$

$$\boldsymbol{K}_{\mathrm{spr3,wswp}} = -k_3 \int_0^{L_x} \partial_y \boldsymbol{\zeta}_{\mathrm{s}}(x, y_{\mathrm{s1}}) \partial_y \boldsymbol{\zeta}_{\mathrm{p}}^{\top}(x, y_{\mathrm{p1}}) \mathrm{d}x - k_3 \int_0^{L_x} \partial_y \boldsymbol{\zeta}_{\mathrm{s}}(x, y_{\mathrm{s2}}) \partial_y \boldsymbol{\zeta}_{\mathrm{p}}^{\top}(x, y_{\mathrm{p2}}) \mathrm{d}x, \tag{B17}$$

$$\boldsymbol{K}_{\mathrm{spr3,wpwp}} = k_3 \int_0^{L_x} \partial_y \boldsymbol{\zeta}_{\mathrm{p}}(x, y_{\mathrm{p1}}) \partial_y \boldsymbol{\zeta}_{\mathrm{p}}^{\top}(x, y_{\mathrm{p1}}) \mathrm{d}x + k_3 \int_0^{L_x} \partial_y \boldsymbol{\zeta}_{\mathrm{p}}(x, y_{\mathrm{p2}}) \partial_y \boldsymbol{\zeta}_{\mathrm{p}}^{\top}(x, y_{\mathrm{p2}}) \mathrm{d}x. \tag{B18}$$

Finally, those of $\boldsymbol{K}_{\mathrm{spr4}}$ become:

$$\boldsymbol{K}_{\mathrm{spr4,usus}} = k_4 \int_0^{L_x} \boldsymbol{\chi}_{\mathrm{s}}(x, y_{\mathrm{s1}}) \boldsymbol{\chi}_{\mathrm{s}}^{\top}(x, y_{\mathrm{s1}}) \mathrm{d}x + k_4 \int_0^{L_x} \boldsymbol{\chi}_{\mathrm{s}}(x, y_{\mathrm{s2}}) \boldsymbol{\chi}_{\mathrm{s}}^{\top}(x, y_{\mathrm{s2}}) \mathrm{d}x, \tag{B19}$$

$$\boldsymbol{K}_{\mathrm{spr4,usup}} = -k_4 \int_0^{L_x} \boldsymbol{\chi}_{\mathrm{s}}(x, y_{\mathrm{s1}}) \boldsymbol{\chi}_{\mathrm{p}}^{\top}(x, y_{\mathrm{p1}}) \mathrm{d}x - k_4 \int_0^{L_x} \boldsymbol{\chi}_{\mathrm{s}}(x, y_{\mathrm{s2}}) \boldsymbol{\chi}_{\mathrm{p}}^{\top}(x, y_{\mathrm{p2}}) \mathrm{d}x, \tag{B20}$$

$$\boldsymbol{K}_{\mathrm{spr4,upup}} = k_4 \int_0^{L_x} \boldsymbol{\chi}_{\mathrm{p}}(x, y_{\mathrm{p1}}) \boldsymbol{\chi}_{\mathrm{p}}^{\top}(x, y_{\mathrm{p1}}) \mathrm{d}x + k_4 \int_0^{L_x} \boldsymbol{\chi}_{\mathrm{p}}(x, y_{\mathrm{p2}}) \boldsymbol{\chi}_{\mathrm{p}}^{\top}(x, y_{\mathrm{p2}}) \mathrm{d}x. \tag{B21}$$

Appendix C: The assembled stiffness matrix

The assembled matrix, $\boldsymbol{K}_{\mathrm{coup}}$, in Eq. (52) has the following entries:

$$\boldsymbol{K}_{\mathrm{usus}} = \boldsymbol{K}_{\mathrm{spr4,usus}}, \tag{C1}$$

$$\boldsymbol{K}_{\mathrm{usup}} = \boldsymbol{K}_{\mathrm{spr4,usup}}, \tag{C2}$$

$$\boldsymbol{K}_{\mathrm{vsvs}} = \boldsymbol{K}_{\mathrm{spr1,vsvs}} + \boldsymbol{K}_{\mathrm{spr2,vsvs}} + \boldsymbol{K}_{\mathrm{spr3,vsvs}}, \tag{C3}$$

$$\boldsymbol{K}_{\text{vsws}} = \boldsymbol{K}_{\text{spr1,vsws}} + \boldsymbol{K}_{\text{spr2,vsws}} + \boldsymbol{K}_{\text{spr3,vsws}}, \tag{C4}$$

$$\boldsymbol{K}_{\text{vsvp}} = \boldsymbol{K}_{\text{spr2,vsvp}}, \tag{C5}$$

$$\boldsymbol{K}_{\text{vswp}} = \boldsymbol{K}_{\text{spr1,vswp}} + \boldsymbol{K}_{\text{spr3,vswp}}, \tag{C6}$$

$$\boldsymbol{K}_{\text{wsws}} = \boldsymbol{K}_{\text{spr1,wsws}} + \boldsymbol{K}_{\text{spr2,wsws}} + \boldsymbol{K}_{\text{spr3,wsws}}, \tag{C7}$$

$$\boldsymbol{K}_{\text{wsvp}} = \boldsymbol{K}_{\text{spr2,wsvp}}, \tag{C8}$$

$$\boldsymbol{K}_{\text{wswp}} = \boldsymbol{K}_{\text{spr1,wswp}} + \boldsymbol{K}_{\text{spr3,wswp}}, \tag{C9}$$

$$\boldsymbol{K}_{\text{upup}} = \boldsymbol{K}_{\text{spr4,upup}}, \tag{C10}$$

$$\boldsymbol{K}_{\text{vpvp}} = \boldsymbol{K}_{\text{spr2,vpvp}}, \tag{C11}$$

$$\boldsymbol{K}_{\mathrm{wpwp}} = \boldsymbol{K}_{\mathrm{spr1,wpwp}} + \boldsymbol{K}_{\mathrm{spr3,wpwp}}. \tag{C12}$$

References

[1] W. C. Hurty, Vibrations of structural systems by component mode synthesis, J. Eng. Mech. Div. 86 (1960) 51–69. https://doi.org/10.1061/JMCEA3.0000162.

[2] W. C. Hurty, Dynamic analysis of structural systems using component modes, AIAA J. 3 (1965) 678–685. https://doi.org/10.2514/3.2947.

[3] G. Gladwell, Branch mode analysis of vibrating systems, J. Sound Vib. 1 (1964) 41–59. https://doi.org/10.1016/0022-460X(64)90006-9.

[4] D. de Klerk, D. J. Rixen, S. Voormeeren, General framework for dynamic substructuring: history, review and classification of techniques, AIAA J. 46 (2008) 1169–1181. https://doi.org/10.2514/1.33274.

[5] R. J. Guyan, Reduction of stiffness and mass matrices, AIAA J. 3 (1965) 380–380. https://doi.org/10.2514/3.2874.

[6] R. R. Craig Jr, M. C. Bampton, Coupling of substructures for dynamic analyses., AIAA J. 6 (1968) 1313–1319. https://doi.org/10.2514/3.4741.

[7] F. J. Fahy, Vibration of containing structures by sound in the contained fluid, J. Sound Vib. 10 (1969) 490–512. https://doi.org/10.1016/0022-460X(69)90228-4.

[8] F. J. Fahy, Response of a cylinder to random sound in the contained fluid, J. Sound Vib. 13 (1970) 171–194. https://doi.org/10.1016/S0022-460X(70)81172-5.

[9] D. Karnopp, Coupled vibratory-system analysis, using the dual formulation, J. Acoust. Soc. Am. 40 (1966) 380–384. https://doi.org/10.1121/1.1910082.

[10] L. Maxit, J. L. Guyader, Estimation of SEA coupling loss factors using a dual formulation and FEM modal information, part I: theory, J. Sound Vib. 239 (2001) 907–930. https://doi.org/10.1006/jsvi.2000.3192.

[11] L. Maxit, J. L. Guyader, Extension of sea model to subsystems with non-uniform modal energy distribution, J. Sound Vib. 265 (2003) 337–358. https://doi.org/10.1016/S0022-460X(02)01459-1.

[12] À. Aragonès, L. Maxit, O. Guasch, A graph theory approach to identify resonant and non-resonant transmission paths in statistical modal energy distribution analysis, J. Sound Vib. 350 (2015) 91–110. https://doi.org/10.1016/j.jsv.2015.04.001.

[13] L. Maxit, O. Guasch, A dual modal formulation for multiple flexural subsystems connected at a junction in energy-based models, Mech. Syst. Signal Pr. 119 (2019) 457–470. https://doi.org/10.1016/j.ymssp.2018.09.038.

[14] L. Maxit, O. Guasch, Energy-based reformulated craig-bampton method for multiple flexural subsystems connected at a junction with low impedance mismatch, Mech. Syst. Signal Pr. 119 (2019) 471–485. https://doi.org/10.1016/j.ymssp.2018.09.039.

[15] Z. Ding, H. Li, G. Zou, J. Kong, Considering higher-order effects of residual attachment modes in free-interface component mode synthesis method for non-classically damped systems, J. Sound Vib. 469 (2020) 115129. https://doi.org/10.1016/j.jsv.2019.115129.

[16] H. He, T. Wang, G. Chen, D. Sun, R. Sun, A real decoupled method and free interface component mode synthesis methods for generally damped systems, J. Sound Vib. 333 (2014) 584–603. https://doi.org/10.1016/j.jsv.2013.09.023.

[17] Z. Ding, L. Li, Y. Hu, A free interface component mode synthesis method for viscoelastically damped systems, J. Sound Vib. 365 (2016) 199–215. https://doi.org/10.1016/j.jsv.2015.11.040.

[18] A. Shanmugam, C. Padmanabhan, A fixed–free interface component mode synthesis method for rotordynamic analysis, J. Sound Vib. 297 (2006) 664–679. https://doi.org/10.1016/j.jsv.2006.04.011.

[19] L. Hinke, F. Dohnal, B. R. Mace, T. P. Waters, N. Ferguson, Component mode synthesis as a framework for uncertainty analysis, J. Sound Vib. 324 (2009) 161–178. https://doi.org/10.1016/j.jsv.2009.01.056.

[20] S.-K. Hong, B. I. Epureanu, M. P. Castanier, D. J. Gorsich, Parametric reduced-order models for predicting the vibration response of complex structures with component damage and uncertainties, J. Sound Vib. 330 (2011) 1091–1110. https://doi.org/10.1016/j.jsv.2010.09.022.

[21] S.-A. Chentouf, N. Bouhaddi, C. Laitem, Robustness analysis by a probabilistic approach for propagation of uncertainties in a component mode synthesis context, Mech. Syst. Signal Pr. 25 (2011) 2426–2443. https://doi.org/10.1016/j.ymssp.2011.04.014.

[22] C. Joannin, B. Chouvion, F. Thouverez, J.-P. Ousty, M. Mbaye, A nonlinear component mode synthesis method for the computation of steady-state vibrations in non-conservative systems, Mech. Syst. Signal Pr. 83 (2017) 75–92. https://doi.org/10.1016/j.ymssp.2016.05.044.

[23] T. Wang, J. He, S. Hou, X. Deng, C. Xi, H. He, Complex component mode synthesis method using hybrid coordinates for generally damped systems with local nonlinearities, J. Sound Vib. 476 (2020) 115299. https://doi.org/10.1016/j.jsv.2020.115299.

[24] A. de Lima, A. da Silva, D. Rade, N. Bouhaddi, Component mode synthesis combining robust enriched ritz approach for viscoelastically damped structures, Eng. Struct. 32 (2010) 1479–1488. https://doi.org/10.1016/j.engstruct.2010.01.028.

[25] H. He, T. Wang, G. Chen, D. Sun, R. Sun, A real decoupled method and free interface component mode synthesis methods for generally damped systems, J. Sound Vib. 333 (2014) 584–603. https://doi.org/10.1016/j.jsv.2013.09.023.

[26] S. M. Kim, J.-G. Kim, S.-W. Chae, K. Park, Evaluating mode selection methods for component mode synthesis, AIAA J. 54 (2016) 2852–2863. https://doi.org/10.2514/1.J054936.

[27] B. Besselink, U. Tabak, A. Lutowska, N. van de Wouw, H. Nijmeijer, D. Rixen, M. Hochstenbach, W. Schilders, A comparison of model reduction techniques from structural dynamics, numerical mathematics and systems and control, J. Sound Vib. 332 (2013) 4403–4422. https://doi.org/10.1016/j.jsv.2013.03.025.

[28] I. Palomba, D. Richiedei, A. Trevisani, Mode selection for reduced order modeling of mechanical systems excited at resonance, Int. J. Mech. Sci. 114 (2016) 268–276. https://doi.org/10.1016/j.ijmecsci.2016.05.026.

[29] B. Starc, G. Čepon, M. Boltežar, The influence of washing machine-leg hardness on its dynamics response within component-mode synthesis techniques, Int. J. Mech. Sci. 127 (2017) 23–30. https://doi.org/10.1016/j.ijmecsci.2016.10.005.

[30] W. Tian, Y. Gu, H. Liu, X. Wang, Z. Yang, Y. Li, P. Li, Nonlinear aeroservoelastic analysis of a supersonic aircraft with control fin free-play by component mode synthesis technique, J. Sound Vib. 493 (2021) 115835. https://doi.org/10.1016/j.jsv.2020.115835.

[31] K. Lu, K. Zhang, H. Zhang, X. Gu, Y. Jin, S. Zhao, C. Fu, Y. Yang, A review of model order reduction methods for large-scale structure systems, Shock Vib. 2021 (2021). https://doi.org/10.1155/2021/6631180.

[32] C. Farhat, M. Géradin, On a component mode synthesis method and its application to incompatible substructures, Comput. Struct. 51 (1994) 459–473. https://doi.org/10.1002/nme.2133.

[33] J. Gerstmayr, J. Ambrósio, Component mode synthesis with constant mass and stiffness matrices applied to flexible

multibody systems, Int. J. Numer. Meth. Engrg. 73 (2008) 1518–1546. https://doi.org/10.1002/nme.2133.

[34] U. L. Hetmaniuk, R. B. Lehoucq, A special finite element method based on component mode synthesis, ESAIM: Math. Model. Numer. Anal. 44 (2010) 401–420. https://doi.org/10.1051/m2an/2010007.

[35] C. Papadimitriou, D.-C. Papadioti, Component mode synthesis techniques for finite element model updating, Comput. Struct. 126 (2013) 15–28. https://doi.org/10.1016/j.compstruc.2012.10.018.

[36] J. Deng, O. Guasch, L. Maxit, L. Zheng, Transmission loss of plates with multiple embedded acoustic black holes using statistical modal energy distribution analysis, Mech. Syst. Signal Pr. 150 (2021) 107262. https://doi.org/10.1016/j.ymssp.2020.107262.

[37] J. Deng, O. Guasch, L. Zheng, Ring-shaped acoustic black holes for broadband vibration isolation in plates, J. Sound Vib. 458 (2019) 109–122. https://doi.org/10.1016/j.jsv.2019.06.017.

[38] L. Tang, L. Cheng, Broadband locally resonant band gaps in periodic beam structures with embedded acoustic black holes, J. Appl. Phys. 121 (2017) 194901. https://doi.org/10.1063/1.4983459.

[39] J. Deng, O. Guasch, L. Zheng, A semi-analytical method for characterizing vibrations in circular beams with embedded acoustic black holes, J. Sound Vib. 476 (2020) 115307. https://doi.org/10.1016/j.jsv.2020.115307.

[40] J. Deng, O. Guasch, L. Zheng, T. Song, Y. Cao, Semi-analytical model of an acoustic black hole piezoelectric bimorph cantilever for energy harvesting, J. Sound Vib. 494 (2021) 115790. https://doi.org/10.1016/j.jsv.2020.115790.

[41] J. Deng, O. Guasch, L. Maxit, L. Zheng, Vibration of cylindrical shells with embedded annular acoustic black holes using the Rayleigh-Ritz method with Gaussian basis functions, Mech. Syst. Signal Pr. 150 (2021) 107225. https://doi.org/10.1016/j.ymssp.2020.107225.

[42] J. Deng, O. Guasch, L. Zheng, Reconstructed Gaussian basis to characterize flexural wave collimation in plates with periodic arrays of annular acoustic black holes, Int. J. Mech. Sci. 194 (2021) 106179. https://doi.org/10.1016/j.ijmecsci.2020.106179.

[43] R. Courant, Variational methods for the solution of problems of equilibrium and vibrations, Bull. Am. Math. Soc. 49 (1943) 1 – 23. https://doi.org/10.1090/S0002-9904-1943-07818-4.

[44] J. Yuan, S. Dickinson, On the use of artificial springs in the study of the free vibrations of systems comprised of straight and curved beams, J. Sound Vib. 153 (1992) 203–216. https://doi.org/10.1016/S0022-460X(05)80002-1.

[45] J. Yuan, S. Dickinson, The flexural vibration of rectangular plate systems approached by using artificial springs in the Rayleigh-Ritz method, J. Sound Vib. 159 (1992) 39–55. https://doi.org/10.1016/0022-460X(92)90450-C.

[46] D. Li, L. Cheng, C. Gosselin, Analysis of structural acoustic coupling of a cylindrical shell with an internal floor partition, J. Sound Vib. 250 (2002) 903–921. https://doi.org/10.1006/jsvi.2001.3959.

[47] J. Missaoui, L. Cheng, M. Richard, Free and forced vibration of a cylindrical shell with a floor partition, J. Sound Vib. 190 (1996) 21–40. https://doi.org/10.1006/jsvi.1996.0045.

[48] S. Ilanko, Penalty methods for finding eigenvalues of continuous systems: Emerging challenges and opportunities, Comput. Struct. 104-105 (2012) 50–54. https://doi.org/10.1016/j.compstruc.2012.02.017.

[49] S. Ilanko, The use of negative penalty functions in constrained variational problems, Commun. Numer. Meth. Eng. 18 (2002) 659–668. https://doi.org/10.1002/cnm.525.

[50] X. Chen, J. Zhao, J. Deng, Y. Jing, H. Pu, J. Luo, Low-frequency enhancement of acoustic black holes via negative stiffness supporting, Int. J. Mech. Sci. (2022) 107921. https://doi.org/10.1016/j.ijmecsci.2022.107921.

[51] S. Ilanko, Introducing the use of positive and negative inertial functions in asymptotic modelling, Proceedings of the

Royal Society A: Mathematical, Physical and Engineering Sciences (2005). https://doi.org/10.1098/rspa.2005.1472.

[52] Z. Wan, X. Zhu, T. Li, J. Fu, A method for improving wave suppression ability of acoustic black hole plate in low-frequency range, Thin-Wall. Struct. 182 (2023) 110327. https://doi.org/10.1016/j.tws.2022.110327.

[53] J. Deng, O. Guasch, L. Maxit, L. Zheng, Annular acoustic black holes to reduce sound radiation from cylindrical shells, Mech. Syst. Signal Pr. 158 (2021) 107722. https://doi.org/10.1016/j.ymssp.2021.107722.

[54] Y. Dong, H. Hu, L. Wang, A comprehensive study on the coupled multi-mode vibrations of cylindrical shells, Mech. Syst. Signal Pr. 169 (2022) 108730. https://doi.org/10.1016/j.ymssp.2021.108730.

[55] J. Deng, O. Guasch, L. Maxit, N. Gao, A metamaterial consisting of an acoustic black hole plate with local resonators for broadband vibration reduction, J. Sound Vib. 526 (2022) 116803. https://doi.org/10.1016/j.jsv.2022.116803.

[56] J. Deng, O. Guasch, L. Maxit, N. Gao, Sound radiation and non-negative intensity of a metaplate consisting of an acoustic black hole plus local resonators, Compos. Struct. 304 (2023) 116423. https://doi.org/10.1016/j.compstruct.2022.116423.

[57] M. Li, J. Deng, L. Zheng, S. Xiang, Vibration mitigation via integrated acoustic black holes, Appl. Acoust. 198 (2022) 109001. https://doi.org/10.1016/j.apacoust.2022.109001.

[58] D. Du, W. Sun, X. Yan, H. Liu, K. Xu, Z. Qin, Modelling and analysis of nonlinear vibrations for a coupling hard-coated ring disc-cylindric shell structure under piecewise-continuous coupling conditions, Int. J. Mech. Sci. 215 (2022) 106940. https://doi.org/10.1016/j.ijmecsci.2021.106940.

[59] J. Deng, N. Gao, L. Tang, H. Hou, K. Chen, L. Zheng, Vibroacoustic mitigation for a cylindrical shell coupling with an acoustic black hole plate using Gaussian expansion component mode synthesis, Compos. Struct. 298 (2022) 116002. https://doi.org/10.1016/j.compstruct.2022.116002.

[60] S. Ilanko, L. Monterrubio, Y. Mochida, The Rayleigh-Ritz method for structural analysis, John Wiley & Sons, 2014.

[61] K. Park, Y. H. Park, Partitioned component mode synthesis via a flexibility approach, AIAA journal 42 (2004) 1236–1245. https://doi.org/10.2514/1.10423.

[62] J. Deng, Y. Xu, O. Guasch, N. Gao, L. Tang, Nullspace technique for imposing constraints in the Rayleigh–Ritz method, J. Sound Vib. 527 (2022) 116812. https://doi.org/10.1016/j.jsv.2022.116812.

[63] J. Deng, N. Gao, Broadband vibroacoustic reduction for a circular beam coupled with a curved acoustic black hole via nullspace method, Int. J. Mech. Sci. 233 (2022) 107641. https://doi.org/10.1016/j.ijmecsci.2022.107641.

[64] J. Deng, Y. Xu, O. Guasch, N. Gao, L. Tang, W. Guo, A wave and Rayleigh–Ritz method to compute complex dispersion curves in periodic lossy acoustic black holes, J. Sound Vib. (2022) 117449. https://doi.org/10.1016/j.jsv.2022.117449.

[65] J. Deng, L. Zheng, P. Zeng, Y. Zuo, O. Guasch, Passive constrained viscoelastic layers to improve the efficiency of truncated acoustic black holes in beams, Mech. Syst. Signal Pr. 118 (2019) 461–476. https://doi.org/10.1016/j.ymssp.2018.08.053.

[66] J. Deng, L. Zheng, O. Guasch, H. Wu, P. Zeng, Y. Zuo, Gaussian expansion for the vibration analysis of plates with multiple acoustic black holes indentations, Mech. Syst. Signal Pr. 131 (2019) 317–334. https://doi.org/10.1016/j.ymssp.2019.05.024.

[67] W. Huang, C. Tao, H. Ji, J. Qiu, Enhancement of wave energy dissipation in two-dimensional acoustic black hole by simultaneous optimization of profile and damping layer, J. Sound Vib. 491 (2021) 115764. https://doi.org/10.1016/j.jsv.2020.115764.

[68] S. Ilanko, S. M. Dickinson, Asymptotic modelling of rigid boundaries and connections in the Rayleigh-Ritz method, J. Sound Vib. 219 (1999) 370–378. https://doi.org/10.1006/jsvi.1998.1847.

[69] S. Ilanko, Existence of natural frequencies of systems with artificial restraints and their convergence in asymptotic modelling, J. Sound Vib. 255 (2002) 883–898. https://doi.org/10.1006/jsvi.2001.4191.

[70] L. E. Monterrubio, Frequency and buckling parameters of box-type structures using the Rayleigh-Ritz method and penalty parameters, Comput. Struct. 104-105 (2012) 44–49. https://doi.org/10.1016/j.compstruc.2012.03.010.

[71] Y. Mochida, S. Ilanko, D. Kennedy, Attaching negative structures to model cut-outs in the vibration analysis of structures, Comput. Struct. 184 (2017) 14–24. https://doi.org/10.1016/j.compstruc.2017.02.003.

[72] H. Askes, S. Ilanko, The use of negative penalty functions in linear systems of equations, Proc. R. Soc. A: Math. Phys. Eng. Sci. 462 (2006) 2965–2975. https://doi.org/10.1098/rspa.2006.1716.